Faculdade de Engenharia

Instituto de Ciências Biomédicas Abel Salazar

Universidade do Porto

Magnetic Responsive Collagen-FeHap$^{2+/3+}$ Coating on Porous Hydroxyapatite Scaffold for Bone Regeneration

Sara Maria Gomes Tiago Madureira

Dissertation for the Integrated Master in Bioengineering

Molecular Biotechnology

Supervisor Dr. Marta de Sousa Laranjeira

Co-Supervisor Prof. Dr. Fernando Jorge Monteiro

September 2021

Abstract

Bone is a complex tissue that serves not only structural, but also important physiological functions. It has an inherent, well-regulated, regenerative capacity, however, in cases of severe fractures and excision surgeries it is often necessary to resort to bone substitutes to achieve optimal healing.

Ceramic and polymeric scaffolds have been extensively studied for their regenerative capacity in many fields. Regarding bone, hybrid scaffolds that combine a hard and a soft material are the go-to since they mimic the natural tissue.

Magnetism is also a great tool for bone regeneration. Scaffolds containing magnetic nanoparticles (MNP) exhibit a magnetic behavior when subjected to external magnetic fields, which modulates osteoblastic adhesion and proliferation, as well as progenitor differentiation, leading to improved osteointegration of the implant in vivo.

In this work, a porous hydroxyapatite scaffold was produced and coated with collagen containing various percentages of superparamagnetic iron doped hydroxyapatite nanoparticles ($FeHap^{2+/3+}$ NPs). The resultant scaffolds presented adequate interconnected porosity (70,8%), satisfactory mechanical properties and were able to form an apatite layer when immersed in simulated body fluid (SBF).

Results obtained in the Resazurin assay showed that scaffolds containing MNP lead to higher metabolic activity of MC3T3-E1 pre-osteoblastic cells, and that this effect could be enhanced through the added influence of a static magnetic field (SMF). Confocal images of actin and nucleus staining imply that the SMF has a detrimental effect on cellular proliferation up to day 7, which might be related to an early differentiation start, triggered by the SMF. Nonetheless, at day 21 this was no longer perceived, and the magnetic field in combination with the MNPs, seemed to enhance the proliferation of the cells when compared with the sample without nanoparticles.

Preliminary studies based on ALP staining also suggest that the materials containing nanoparticles support osteogenic differentiation, when in comparison with the control scaffold, without MNPs. The effect of the magnetic field in this assay was not evident. These findings suggest that the novel magnetic responsive scaffolds may be suitable candidates to be used for bone regeneration purposes.

(page intentionally left blank)

Acknowledgements

Firstly, I would like to thank my supervisor, Dr. Marta Laranjeira, for always supporting my ideas, for the help accomplishing them and for the calming words in moments of stress.

A big thanks goes to Prof. Dr. Fernando Jorge Monteiro for accepting me into the Biocomposites Group at i3s and to all the team for welcoming me. I also need to express my gratitude towards Ângela Carvalho and Tiago Ribeiro for all the support, advice and help given throughout this work, and towards Joana Barros, for always making me laugh and unwind from work.

I must thank my parent for always having allowed me to choose my path and supporting me in every step of it. To Zé, for always being there to listen and for reassuring me that everything would be fine when nothing seemed to work in my favor.

Finally, I want to acknowledge every Professor and colleague that crossed my path in the last three years in MIB and contributed for my personal and professional growth.

(page intentionally left blank)

Contents

(page intentionally left blank)

Figure List

(page intentionally left blank)

Abbreviations

ALP Alkaline Phosphatase

BCP Biphasic Calcium Phosphate

BMP Bone Morphogenic Protein

BMU Basic Multicellular Unit

CaP Calcium Phosphate

COL Collagen

CT Computerized Tomography

DLS Dynamic Light Scattering

ECM Extracellular Matrix

EDC 1-ethyl-3-(3-dimethylaminopropyl)carbodiimide hydrochloride

FBS Fetal Bovine Serum

FeHap$^{2+/3+}$ Iron (II and III) Doped Hydroxyapatite

FTIR Fourier-Transform Infrared Spectroscopy

Hap Hydroxyapatite

HSC Hematopoietic Stem Cells

LDH Lactate Dehydrogenase

MES 4-Morpholineethanesulfonic acid

MNP Magnetic Nanoparticle

MSC Mesenchymal Stem Cell

NHS N-Hydroxysuccinimide

NP Nanoparticle

OPG Osteoprotegerin

PCL Phosphorus Trichoride

PEG Polyethylene glycol

PEMF Pulsed Electromagnetic Field

PGA 3-Phosphoglyceric Acid

PHA Polyhydroxyalkanoate

PLA Polylactic Acid

PLGA Poly(lactic-co-glycolic acid)

PLLA Poly(L-lactide acid)

SBF Simulated Body Fluid

SMF Static Magnetic Field

SPION Superparamagnetic Iron Oxide Nanoparticle

SQUID Superconducting Quantum Interference Device

TC Tropocollagen

TCP Tricalcium Phosphate

TEM Transmission Electron Microscopy

XRD X-ray Diffraction

1. Introduction

1.1. Bone Tissue

1.1.1. Bone Morphology

Bone is a complex and dynamic tissue made of a unique combination of materials arranged in a 3D network. Apart from its main function of proving structural support, the skeleton is also the place where hematopoiesis occurs, it serves as a reservoir for minerals (such as Ca and P ions) and nutrients, and protects our internal organs[1–3].

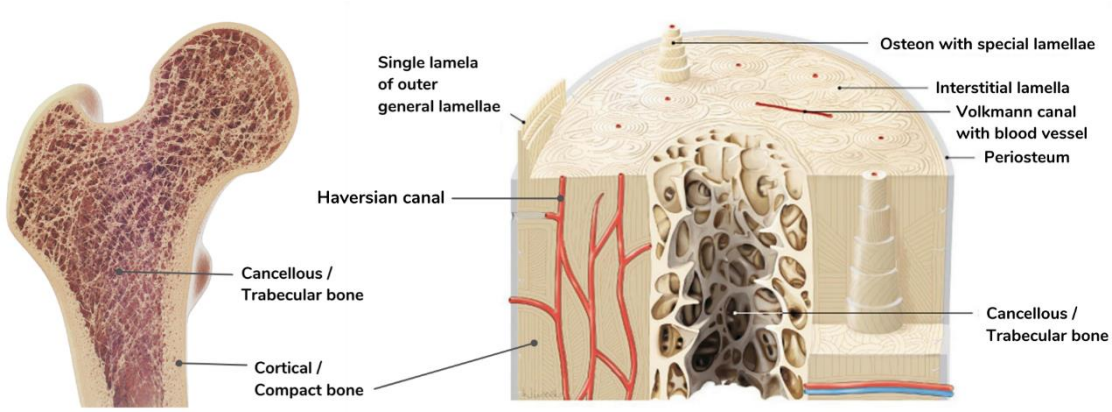

Figure 1. Cross sectional representation of cortical and cancellous bone. Bone marrow can be found within the cavities of cancellous bone. Cortical bone is formed by tightly packed osteons, which are formed by Haversian canals - that comprise blood vessels and nervous tissue – and lined by concentric lamellae. Adapted from [4] and [5].

Bone tissue presents two distinct architectures, compact and trabecular[4,5].

Compact or cortical bone can be found in long (femur), short (wrist bones) and flat bones (skull), making up 80% of the skeleton. It is located on the outer layer of the bone, exhibits the bone vasculature and is covered by a denser outermost layer, the periosteum. It is responsible for the release of minerals when facing a deficiency and for bone's structural integrity, due to its high density (with only 10% porosity) and its extensive net of collagen fibrils [1,6]. This architecture is accountable for the high torsional resistance of cortical bone [7].

Trabecular bone (also called spongy or cancellous), surrounds the bone marrow in long bones and fulfills the vertebral bodies. This tissue is highly porous (50 to 90% porous) and it is organized in interconnected branches that give the appearance of a honeycomb-like structure. This organization makes it less resistant than cortical bone, however, trabecular bone has a great impact on the structural integrity of the tissue. Moreover, its vast surface area is essential for the occurrence of metabolic processes and bone turnover[1,6]. It is within the trabeculae that bones blood vessels ramify, and mesenchymal and hematopoietic stem cells reside (MSC and HSC, respectively).

Bone cells (to be discussed ahead) are surrounded by an extracellular matrix with an inorganic phase, mainly composed of hydroxyapatite, and an organic phase, with type I collagen fibers (around 90%), non-collagenous proteins, lipids and water [3,7].

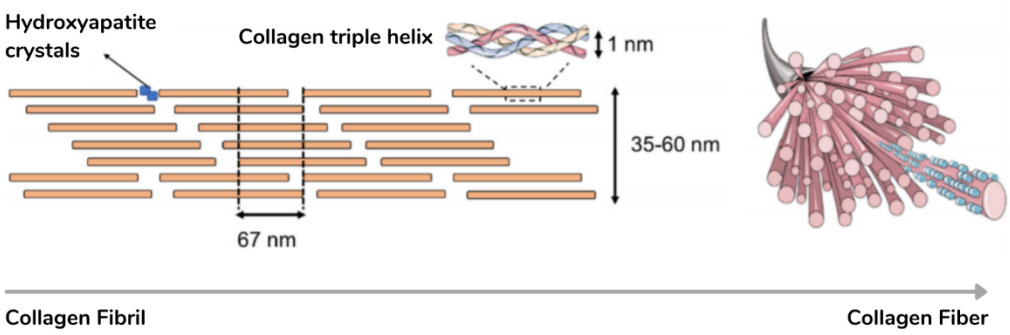

Figure 2. Collagen hierarchical organization in bone's extracellular matrix. Adapted from [2].

In the matrix, collagen triple helices, or tropocollagen (TC), are self-organized in fibrils with diameters varying from 35 to 60 nm and length of approximately 1 µm. The interstices between TC serve as nucleation sites for hydroxyapatite crystals that mineralize and fortify the matrix[2,8], which ultimately give rise to the higher hierarchical structure, the collagen fiber (~10 nm). Bone's mechanical properties such as resilience and strength depend on the 3D structure adopted by the collagen fibrils, as well as their conformational relationship with Hap crystals[8].

Besides collagen, non-collagenous proteins, as osteocalcin, osteonectin and osteopontin; adhesion proteins, like fibronectin and vitronectin; and proteoglycans are

crucial for the stability of the ECM and for the regulation of collagen mineralization and cell behavior through the delivery of biochemical signals[9].

1.1.2. Bone Cells

Osteoblasts derive from a multipotent mesenchymal progenitor cell (MSC), through a cascade mechanism involving the transcription factors Runx2 and OSX (osterix), as well as proteins from the BMP family[1,2,7]. These cells have a cuboidal shape and are located at the bone surface, forming a tightly organized cell layer. Osteoblasts secrete type I collagen, proteoglycans and glycoprotein and are, therefore responsible for the synthesis of new bone matrix[10].

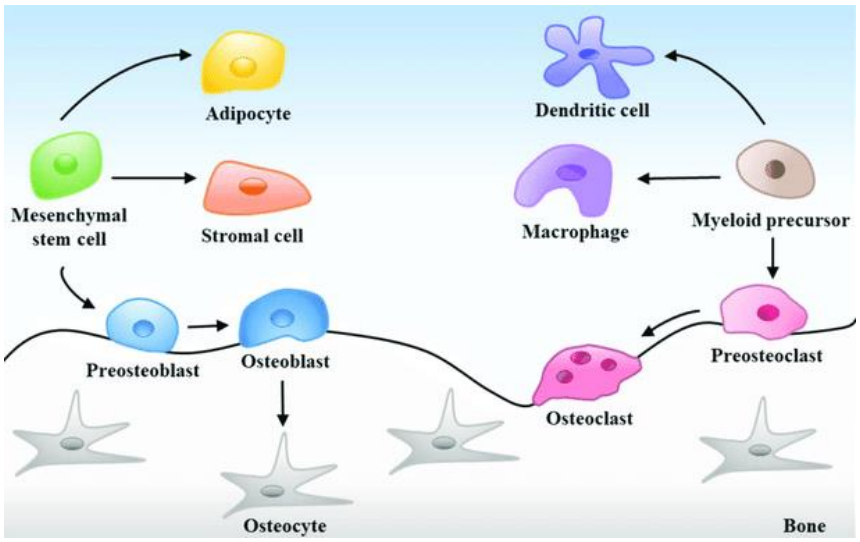

Figure 3. Squematic representation of bone cells and their differentiation routes. Adapted from [9].

During the process of new bone formation, osteoblasts can get entangled and entrapped in the newly calcified matrix. Afterwards, when matured and fully differentiated, these cells become osteocytes. When the conditions are not met for osteoblasts to differentiate into osteocytes, they can become a bone lining cell, or go into apoptosis [7].

Osteocytes reside in the osteon, inside the lacuna, and comprise over 90% of cells in the adult bone. These cells exhibit dendritic configuration with cytoplasm ramifications that serve as connection between osteocytes and with the osteoblasts that

reside on the surface of bone. Osteocytes are also bone's mechanosensors, sending load and stress signals that can regulate osteoblast and osteoclast activity[7].

Osteoclasts derive from a myeloid precursor, like macrophages or dendritic cells, however, they are larger and multinucleated, since they arise from the fusion of mononucleated precursors. These are the only cells able to dissolve the mineral part of bone matrix, as well as digest it, playing a critical role in the bone remodeling cycle. They achieve this by acidification of the surrounding medium and secretion of proteases (to dissolve the organic phase).[1,6,11]

Besides from the main bone cells described, there are other cells that have a contribution to bone modeling and remodeling such as chondrocytes and bone lining cells, as well as HSC and MSC, that are confined in the bone marrow.

1.1.3. Bone Remodeling Cycle

Bone tissue is constantly being reconstructed throughout our lifespan. During childhood and adolescence, bone undergoes a continuous process of longitudinal and radial growth, known as bone modeling. During adulthood, bones mainly suffer remodeling[2]. Osteoclasts and osteoblast take the lead in this process, since the first resorbs bone matrix, and the last secretes it [7]. It is crucial to have perfect balance between these two actions, in order to maintain mineral homeostasis and the structural integrity of bone tissue, while making sure any damages are being repaired and hyper-mineralized areas destroyed.

The bone remodeling cycle has five phases: activation; resorption; reversal; formation; termination, and occurs in a temporarily restricted zone named the basic multicellular unit (BMU), that is delimitated by bone lining cells[7].

Remodeling of adult bone is commanded by osteocytes. When osteocytes go into apoptosis due to bone matrix damage, paracrine factors such as RANKL are released. RANKL finds its receptor (RANK), present in osteoclast precursor cells, recruited from the circulation to the BMU. Bone lining cells form a canopy over the area of the bone where the remodeling is going to take place (Activation phase)[7].

After this event, precursor cells differentiate into osteoclasts, that dissolve bone minerals (through a proton pump generated by Carbonic Anhydrase II) and collagen

matrix (by proteases and metalloproteinases). The phase between resorption bone matrix and formation of new bone (Reversal phase) is where the bone surface that suffered resorption is prepared for osteoblastic adhesion, with the deposition of a mineralized matrix layer[7].

In the Formation phase, osteoblasts first secrete a type-I collagen matrix and are then involved in the process of regulating matrix mineralization. After this event, osteoblast follow one on the routes addressed above, differentiation into osteocytes or apoptosis (Termination).

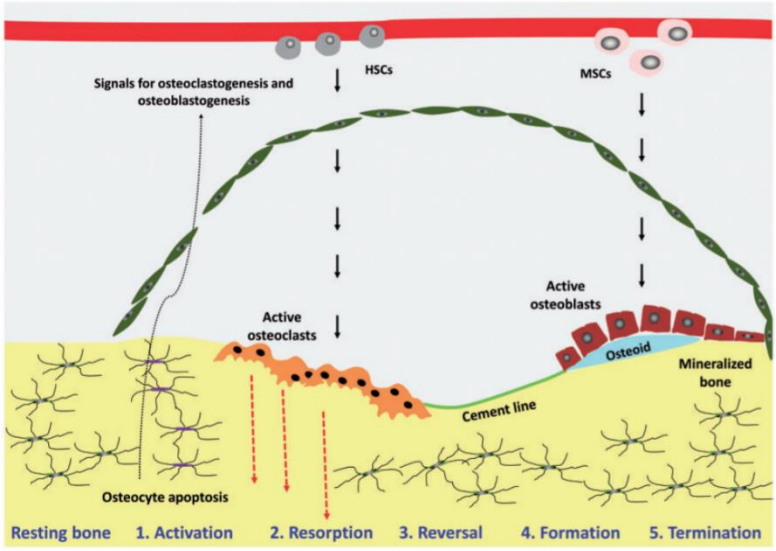

Figure 4. Schematic representation of bone remodeling cycle. Adapted from [7].

As was explained, the release of RANKL, and consequent coupling with RANK, is the main stimulus that induces bone remodeling. For the regulation between resorption and bone formation, OPG (osteoprotegerin), secreted by osteoblasts and osteocytes, is crucial since it can also bind to RANKL, inhibiting osteoclast activation.

1.2. Bone Regeneration Approaches

After a traumatic event, bone tissue attains full regeneration with scarce or no scar formation, restoring its original structure and mechanical characteristics, such as its load bearing capacity and fracture toughness. However, this is only true for mild injuries or small fractures. After a certain size (critical size injury), the regenerative capacity of

bone is no longer sufficient and there is the need to use a bone graft[3,12,13]. Critical size injuries are mainly associated with a traumatic event that resulted in a nonunion fracture or the necessity of bone resection due to tumors or severe infections. In dentistry, bone grafts are also used to fill ridge defects before the insertion of implants.

Several types of bone grafts can be used in the clinic, from autografts, allografts and xenografts to a wide range of bioengineered substitutes made of natural and synthetic materials. Briefly, a bone graft should promote osteogenesis, osteoinduction and osteoconduction[14] when applied alone or combined with other materials.

An osteoconductive material possesses an internal architecture that facilitates new bone formation. Osteoinduction depends on an active stimulation of bone formation through the release of growth factors or ions that constitute the biomaterial (calcium phosphates, for example, release ions to the surrounding medium, that are important for the deposition of new apatite)[15]. As for osteogenesis, it relates to the inherent capacity of the material to promote cell adherence, proliferation and osteoblastic differentiation, or to produce mechanical stimulus through stress-relaxation patterns[15].

From the above mentioned, only autografts gather the three characteristics when used alone, furthermore, they will not transmit diseases or induce immune response, since they are harvested from an autologous source[13]. Despite being the "gold standard" in the treatment of small bone injuries, autografts present some disadvantages such as the pain and morbidity inherent to the donor site as well as the need for longer and multiple site surgeries that require general anesthesia[16,17].

These drawbacks open the way for optimized engineered materials that mimic bone structure and properties, promoting the regenerative ability of the surrounding tissue while presenting low rejection responses[18].

1.2.1. Biomaterials for Bone Regeneration

When addressing biomaterials for tissue regeneration it is important to design them in a way that mimics the intrinsic characteristics of the target tissue[14].

The materials used to construct a scaffold for bone regeneration will determine its hydrophobicity, surface tension, solubility and biodegradability, while its design and construction method will influence the amount of pores in the scaffold, as well as the shape, average size and interconnectivity of the pores, crucial characteristics when seeking osteoconduction and angiogenesis after implantation[13,19,20].

1.2.2. Ceramic Materials

Many studies on this matter resort to scaffolds made of calcium phosphates since they resemble natural bone apatite[21,22], lead to efficient osteointegration of the scaffold and are of easy access since many forms of CaPs are commercially available[13,21,22]. Calcium phosphates are composed of calcium (Ca^{2+}), phosphorus (P_5^+) and oxygen (O_2^-) and can be divided into different categories: orthophosphates, metaphosphates, pyrophosphates, triphosphates and tetraphosphates – PO_4^{3-}, PO_3^-, $(P_2O_7)^{4-}$, $(P_3O_{10})^{5-}$ and P_4O_{13}, respectively.

For bone regeneration purposes, calcium orthophosphates are the most exploited since they exist in the inorganic phase of bones and teeth[23–25]. Calcium phosphate-based materials contribute to bone regeneration primarily due to the release of calcium and phosphate ions resulting from the material's degradation when in contact with body fluids. The increased concentration of these ions in the medium leads to extended protein adsorption to the material, that results in further dissolution of ions and ultimately, their reprecipitation, with new bone formation.[26–28]

Hydroxyapatite, $Ca_{10}(PO_4)_6(OH)_2$, is a hydrated calcium phosphate that results from biomineralization in bone tissue formation. Briefly, after collagen is secreted by osteoblasts, nucleation of Hap crystals starts within the collagen fibers, resulting in the mineralized fibers. Synthetic Hap has been widely studied for bone replacement purposes due to its wide similarities with natural bone[29,30], such as its calcium to phosphorus ratio (approximately 1.67), and because it is thermodynamically stable at pH 4.3 and above (which includes the physiological pH, 7.4)[31,32]. Likewise, it is a bioactive ceramic with interesting osteoconductive properties[33]. Bone implants and fillers

composed of hydroxyapatite show good stabilization and fixation to the adjacent tissues, with formation of new biologically active carbonate apatite layer[31].

However, Hap has high crystallinity and chemical stability[34,35], making its degradation a challenge for both multinucleated cells and physiological fluids[34,36]. Furthermore, the brittle nature of Hap makes it unsuitable to be used in weight supporting locations[37,38].

There is also great focus on tricalcium phosphates and biphasic calcium phosphates[39] for bone engineering purposes. Both crystalline phases of tricalcium phosphate ($Ca_3(PO_4)_2$), β-TCP and α-TCP, similarly to Hap[33], present biocompatibility and osteoconduction characteristics, moreover, they have higher solubility due to their lower calcium/phosphate ratio[3], hence faster degradation in vivo, allowing for easier substitution of the scaffold for new bone[40–42]. The chemical composition of the polymorphs is not influenced by the heat, however, the structural changes generated during the process make their density and solubility differ[43] - α-TCP dissolves faster than β-TCP in vitro and in vivo, therefore, it is more biodegradable[42,43]

When aiming for specific solubility conditions, biphasic calcium phosphates are highly interesting for bone regeneration purposes. BCPs consist of a mixture of Hap and β-TCP sintered at temperatures above 700°C[44]. Since both the HA/β-TCP ratio and the sintering temperature are tunable, it is possible to achieve a biocomposite with optimal bioreactivity[45].

1.2.3. Hybrid Materials

As described above, bone is a complex tissue, comprising an organic and inorganic phase. Therefore, a biomaterial intended to function as a bone graft should incorporate these two phases to better mimic the original tissue.

Calcium phosphate ceramic scaffolds are comparable to the inorganic part of bone, they are biocompatible, osteoconductive and present many other advantages for the construction of biomaterials for bone regeneration as described in the previous

section. However, their brittle nature restricts the purposes in which they can be applied[46,47].

Natural polymers such as collagen, chitosan and hyaluronic acid[13,48] that resemble bone's organic phase (some are even present in natural bone ECM, the glycosaminoglycans) can also be used in the production of scaffolds for bone tissue engineering, just as synthetic polymers like PLA, PLGA, PHA and PGA[49–52]. Such polymers, though, have poor mechanical properties when used alone[53], they can suffer deformation after synthesis and shrinkage when cultivated with cells in vitro[54] and even when implanted in vivo[55].

Both natural and synthetic polymers can be combined with CaPs to achieve an optimum hybrid bone graft. Regardless of whether the polymers are used as the scaffold matrix with embedded ceramic particles or used as a coating layer over a hard scaffold, results show improved features when compared to one component biomaterial. The resultant composite materials normally present enhanced structural integrity and flexibility when compared to solely ceramic materials[56].

Many studies focus on combining Hap and TCPs with collagen when designing scaffolds for bone engineering, since this is the main component of bone's extracellular matrix[57].

Tebyanian et al. (2019) described that, when implanted onto rabbit calvaria bone defects (with 8mm diameter), scaffolds made of type I collagen and β-TCP showed immature bone formation after 4 weeks of implantation and, after 8 weeks, new bone was already bridging the defects. On the other hand, in defects treated with scaffolds made solely of collagen, cell penetration onto the scaffolds was delayed, and bone formation only started to occur around week 8. Also, the addition of β-TCP in the scaffold matrix resulted in higher vascularization and improved mechanical properties when compared with COL-scaffolds[55].

A previous study had obtained similar results with nano-Hap/PCL scaffolds, where the presence of hydroxyapatite in the scaffolds improved its mechanical properties with no adverse effect on the biocompatibility of the construct. The nano-Hap/PCL material showed higher osteoblastic proliferation and differentiation both in

vitro and in vivo when compared to PCL scaffolds thus leading to enhanced osteogenesis of bone defects when treated with this hybrid material[58].

As adding ceramic component onto a polymeric scaffold enhances its mechanical properties, the contrary is also true. Milovac et al. (2013) coated a porous hydroxyapatite scaffold with PCL using vacuum impregnation. The resultant scaffolds maintained the interconnectivity of the pores but with enhanced elasticity and strength, therefore, allowing it to be used in locations associated with higher stress, where basic Hap scaffolds would be compromised[59].

1.3. External Cues for Osteointegration

The effect of biophysical stimuli on cell proliferation and differentiation has been a study subject of interest in many fields of regeneration. When a scaffold is implanted onto an osseous region, the final intent is the osteointegration of the implant and its success depends on how different cues are sensed by the cells adjacent to the implant, transferred to the surrounding cells and also, on the cell's response to these signals[60–63]. Despite many options available for bone substitutes, there are still downsides inherent to all of them, such as the insufficient angiogenesis in the middle of the scaffold or the poor mineralization of the newly formed tissue[64–66].

The construction method chosen will dictate the scaffolds architecture that, in turn, will act as an internal cue for cells. Furthermore, the degree of resemblance to the natural extracellular matrix of the interest tissue has a serious impact on cells behavior and response to the implant[64,67].

There are many categories of external triggers that can be used to modulate cell response, both physical and biological. Mechanical stimuli, such as load bearing, dynamic compression, and fixation methods (internal or external) are some of the physical parameters that have been studied in order to achieve optimal response after fracture[63]. On the other hand, growth factors and other molecules can be used as biological cues[68]. In the clinic, local therapy with BMP is already used in surgical context, as well as infection therapy with antibiotic loaded cements[15].

Physical cues, like the ones resultant from daily locomotion, cause tension within the bone tissue, causing it to remodel as a response of that applied stress. This process of transforming biophysical stimuli in a biochemical signal is known as mechanotransduction[69].

1.3.1. Electric and Magnetic Cues

Electric and magnetic stimulation are, likewise, of great relevance for research in regenerative engineering[70]. Low intensity pulsed ultrasounds (LIPU), low intensity high frequency vibration (LIHFV), low power direct current (LPDC) and the application of electromagnetic fields are some of the different approaches available for applying external magnetic stimuli on tissues[63]. Static magnetic fields and pulsed electromagnetic fields are discussed in many studies concerning bone repair and regeneration. They provide a tunable signal to osteoblasts and progenitor cells, leading to a molecular response that will stimulate osteoblastic proliferation and differentiation of the progenitor cells, as well as, in some cases, inhibition of osteoclast activity[71,72].

Pulsed electromagnetic fields are proven to enhance bone formation when applied for one hour a day during 8 weeks after fracture of canine mid-tibia, increasing mechanical strength and weight bearing capacity of the injured limb[73]. Moreover, double-blind studies in humans have verified its benefits after fracture events and osteotomy surgery[74]. Nowadays, however, SMF seems to be the norm in most in vitro and in vivo studies regarding bone repair, probably due to the fact that they are easier to implement in laboratory context.

Static magnetic fields can be divided into four categories given their intensity. Therefore, intensities lower than 5 μT make for a hypo-magnetic field (lower than the geomagnetic field felt on earth); from 5 μT–1 mT are entitled weak SMFs; moderate magnetic fields range from 1 mT to 1 T; and finally, for intensities higher than 1 T, high SMF[75,76]. Low and moderate static magnetic fields are not harmful for animals and humans, in contrast to hypo and high SMF[77], and, since they can be induced by a permanent stationary magnet, are of easy application in the lab as well as in the clinic[75].

In the context of bone repair, moderate SMFs have shown advantages to the bone regeneration process, accelerating the recovery period and giving rise to a denser osseous mineral phase after fracture and graft implantation in several animal species[49,50,78–80].

1.4. Magnetic Biomaterials

Different forms to use magnetism to optimize bone regeneration have been described and investigated. Cells respond to electric and magnetic fields, hence, these can be used to regulate cell behavior, through modulation of cell adhesion and proliferation, reorganization of the cytoskeleton, accelerate bone formation/mineralization, up or down regulation of specific genes and to control and guide cells differentiation[33-36,44, 54–57,61–65].

Magnetic stimulation can be applied not only through external magnetic fields (static or dynamic), but also through the incorporation of magnetic nanoparticles onto bone scaffolds.

1.4.1. Magnetic Nanoparticles

The number of purposes for magnetic nanoparticles in the biomedical field has increased steadily over the years due to their paramagnetic and superparamagnetic behavior (observed in iron oxide based NPs[84]). The most studied MNPs for this purpose are composed of iron oxide phases such as magnetite (Fe_3O_4), maghemite (γ-Fe_2O_3) and hematite (α-Fe_2O_3)[85,86]. These oxides, when in bulk, present a ferromagnetic (magnetite and maghemite) or antiferromagnetic (hematite) behavior, meaning that, once subjected to an external magnetic field, the magnetization lingers for some time after the field is removed. However, when these materials are presented in a nanoscale (normally between 20 and 150 nm) their magnetic profile shifts to superparamagnetic, therefore, their magnetization ceases alongside with the magnetic field[85].

The magnetic behavior of these superparamagnetic iron oxide nanoparticles (SPIONS) is very interesting in the clinic, since it can be used to guide the NPs towards their target after they are in the bloodstream. These particles have low cytotoxicity and

therefore can be used as contrast agents in biomedical imaging, as drug delivery vehicles, to induce hyperthermia in cancer treatment, among other applications[87–90].

Despite being relatively safe, the long-term physiological effects of magnetite and maghemite for humans are not fully understood to this day. Having this in mind, there has been an attempt to produce superparamagnetic nanoparticles that are biocompatible and bioresorbable by doping hydroxyapatite with iron[86,91].

In fact, many ions have been introduced in the lattice of hydroxyapatite (Mg^{2+}, Zn^{2+}, Sr^{2+}, Fe^{2+}, F^{-}, CO_3^{2-}) by anionic and cationic substitution of calcium ions (Ca^{2+})[92,93]. These substitutions result in specific differences in the characteristics of the final molecule and are only possible due to the flexible structure of Hap[94].

In this case, the cationic substitution of calcium with Fe^{2+}, Fe^{3+}, or both, induces deformations in the Hap lattice, and alters the magnetic properties of the material, from diamagnetic (pure Hap), to superparamagnetic (iron doped Hap)[94]. Also, FeHap can have enhanced thermal stability and mechanical properties, higher bioactivity and resorbability, different grain size, and even promote the adhesion of cells, such as osteoblasts[91,94].

1.4.2. Magnetic Scaffolds in Bone Regeneration

Scaffolds that incorporate magnetic nanoparticles can influence cell behavior due the MNP's inherent capacity of giving rise to a static nano magnetic field[95]. To design a magnetic scaffold, aspects such as which materials can be combined and what percentage of nanoparticles should be used are decisive to the success of the material.

Singh et al. (2014) developed a thorough description of behavioral characteristics of PCL fibrous scaffolds prepared by electrospinning, containing 5, 10, 15 and 20% of magnetite NPs. The overall properties of the material were improved by the addition of MNPs, as was expected. However, while the ascent from 5% to 15 % showed improved traits, when the amount of NPs reached 20%, the PCL nanofibers suffered a size increase, result of the agglomeration of the nanoparticles in the PCL dispersion which impaired

the electrospinning process[52]. Therefore, the percentage of magnetic nanoparticles used in the matrix of these scaffolds can be limited by the construction method used.

In another study, the same type of MNPs were introduced in the production of a hydroxyapatite scaffold, comprising 5, 10 and 50% of the total material. In this case the percentage of NPs used was not limited by the construction method itself, since these scaffolds were prepared by a foaming technique. However, after the sintering step, hematite was found in the scaffold initially containing 50% of MNPs. In this scaffold, the magnetization measured under high magnetic fields decreased, when compared to the 10% magnetite scaffolds. This is due to the different specific magnetization presented by magnetite and hematite[79]. Thus, the attempt of producing a scaffold with higher content in magnetic nanoparticles lead to a lower magnetic potential of the final construct.

Concerning in vitro studies, scaffolds composed of either ceramic or polymeric materials have osteoinductive properties when incorporated with magnetic nanoparticles. In general, these scaffolds are composed of approximately 10% MNPs and enhance osteoblast adhesion and proliferation, as well as the differentiation of progenitor cells. These effects can yet be amplified with static magnetic fields, which vary from 1 mT to 320 mT, depending on the experiments[50–52,79,96].

Kim et al. (2015) studied the behavior of bone marrow derived MSCs under the influence of static magnetic fields with three different intensities within the moderate SMF range: 3, 15 and 50 mT[97]. Since mesenchymal stem cells are the precursors to osteoblast like cells[98], it is important to evaluate their response to a magnetic environment when we intend to use magnetism as a stimulus for bone regeneration. The group concluded that the SMF leads the MSC to differentiate into osteoblast and to proliferate in culture, moreover this behavior was supported by the up-regulation of genes related to calcium binding proteins and bone mineralization. The field intensity that resulted in a better cell response was 15 mT[97], which is somewhat contradictory to other studies, where excellent results were obtained using much higher intensities both on MSC and osteoblastic cells[50,69]. This may be justified by the fact that in this study, the cells were not seeded onto a 3D scaffold but rather on a 2D culture medium.

When magnetic scaffolds are implanted on animal models, such as mice, rats, rabbits and even dogs, the osteointegration of the implant is faster and more efficient than when non-magnetic scaffolds are used[50,79,80]. Evaluation on the implanted site shows more vascularization and a neu tissue with denser mineralization. Likewise seen in cellular studies, when a magnetic field is applied after surgery (for 4, 8, 16 weeks, depending on the study), the regeneration occurs even faster than without SMF.

Yun et al. (2016) developed an investigation in order to understand if simultaneous use of magnetic scaffolds and magnetic fields had a cumulative effect on bone repair and regeneration. Initially, a PCL scaffold with magnetic nanoparticles was produced and cultured with mouse osteoblasts. The results of gene expression quantification of transcription factors for osteoblast differentiation (Runx2 and Osterix) showed 5% enhancement for the magnetic scaffolds and 10% when these were combined with SMF. The activity of a biochemical marker recognized for early osteoblastic activity (ALP) was also measured and appeared slightly increased in the magnetic scaffold samples and highly increased when SMF was applied. Since the interaction between the cells and the ECM is so important for cell migration and differentiation, integrin pathways such as FAK, paxillin and RhoA were studied, showing activation by the magnetic scaffold and magnetic field[78].

As expected, the in vivo results showed an optimization of bone formation and repair capacity, with 1.9 times more bone formation observed in magnetic scaffolds with 10% MNPs when compared to non-magnetic scaffolds. When SMF was applied, the bone formation was 2.7 times higher than in the control (1.4 times higher than without magnetic field)[78].

A more recent study[50] showed similar results related to transcription factors expression and ALP activity, as well as integrin pathway activation. Moreover, the in vivo results also showed collagen production enhancement. This study used higher magnetic fields in the in vivo study, accompanied by a lower percentage of MNPs in the scaffold's composition.

These two parameters, percentage of MNP and intensity of SMF can be altered to achieve optimal results. The composition of the scaffold and the nature of the

nanoparticles also influences the overall magnetic capacity of the material and, therefore, its influence on cells and tissues.

Another approach for exploiting the benefits of magnetism for bone regeneration is to introduce magnetic nanoparticles in a polymeric layer coating the implant. This was the premise of Zhuang Junjun and his team. In their work, a titanium surface was coated with mineralized collagen containing magnetite nanoparticles. The application of a SMF caused the coating layer to expand and contract, giving rise to an internal mechanical stimulus, sensed by the cells surrounding the implant. Hence, mechanical stimuli triggered the up-regulation of osteoblast differentiation related genes and the activity of a series of proteins that ultimately resulted in enhanced differentiation of MC3T3-E1 cells[99].

The deformation that occurs in polymeric materials containing magnetic nanoparticles (ferrogels) when stimulated by an external magnetic field is a highly interesting trait, not only to be used as mechanical cell stimulation in tissue regeneration, but also as an on-demand drug release implantable system[100].

1.5. Conclusions

Engineered bone grafts are paving their way into regenerative medicine due to their highly tunable characteristics. The scientific community is always trying to improve the existing scaffolds, both by optimizing their construction techniques and by experimenting with different materials.

For many years, electric and magnetic fields have been implemented in several studies concerning the regenerative capacity of different tissues. In bone regeneration, magnetic fields have shown excellent results by improving osteoblastic adhesion and proliferation, as well as mesenchymal stem cell differentiation into osteoblast like cells.

Besides the application of external magnetic fields, we have seen that the incorporation of magnetic nanoparticles in the construction of bone scaffolds can lead to a more efficient cell behavior towards osteointegration. Moreover, the combined effect of internal and external magnetism leads to amplified benefits.

Magnetic scaffolds can be very promising, however, there are still some barriers to overcome. For example, the percentage of MNPs used is limited by the construction method of the scaffold. When a scaffold is assembled by electrospinning or bioprinting, the nanoparticles in solution/ink tend to aggregate, interfering with the diameter of the resultant fibers and the porosity of the scaffold. Additionally, the conclusions regarding SMF intensities that can be applied and that exhibit optimal cell response are not consistent. Possibly, distinct cell types and animal species respond differently to the magnetic stimuli, or maybe that variability arises from the different scaffolds and how the cells interact with it.

Nonetheless, the role of magnetism in bone regeneration cannot be denied. Magnetic scaffolds have proven their worth both *in vitro* and *in vivo* studies, with and without an external magnetic field source. Moreover, the possibility of combining drug delivery options to these materials allows for a wide range of clinically relevant features.

1.6. Aim

The aim of this thesis was to develop a novel biomaterial with magnetic properties with the potential to promote progenitor proliferation, osteoblastic differentiation and ultimately, bone regeneration.

With this objective, iron doped hydroxyapatite nanoparticles ($FeHap^{2+/3+}$) were synthesized by chemical precipitation and characterized. These magnetic nanoparticles (MNP) were dispersed in a collagen solution with different mass ratios of collagen/nanoparticles content (1/0, 1/0.5, 1/1 and 1/1.5).

Further on, porous hydroxyapatite scaffolds were produced by sponge impregnation, and sintered at 1300 °C. The described collagen solutions were applied dropwise on the Hap scaffolds and collagen was crosslinked. In this step were produced four different scaffolds with crescent nanoparticle content: 0MNP, 0.5MNP, 1MNP and 1.5MNP.

Scaffolds characterization was performed to confirm that characteristics such as porosity, mechanical strength, collagen distribution and apatite deposition capacity were within the expected for a material to be used for bone substitution.

Finally, biological studies were made to assess the effect of the increasing concentrations of MNPs on cell behavior, as well as the potential of an external magnetic field in enhancing these effects.

2. Materials and Methods

2.1. Materials and Reagents

For the magnetic nanoparticle's synthesis, calcium hydroxide (98%), iron II chloride tetrahydrate (99+%), iron III chloride hexahydrate (99+%) and phosphoric acid (85% in water) were purchased from Acros Organics, USA.

For the scaffold fabrication, the polyurethane sponge SupraCell AR 4234 BR, the hydroxyapatite nanoXIM·HAp202, and the dispersant Dolapix CE64 were kindly provided by Euroespuma, Portugal; Fluidinova SA, Portugal; and Zschimmer & Schwarz, Germany, respectively. Type I collagen (bovine Achilles tendon), MES and NHS were purchased from Sigma-Aldrich, USA and EDC from Fluka.

For cell culture purposes, α-MEM medium, fetal bovine serum (FBS), fungizone, penicillin-streptomycin and trypsin were purchased from Gibco (Thermo Fisher Scientific, USA).

ALP staining was achieved with Fast Blue RR Salt and α-Naphthyl phosphate disodium salt, purchased from Sigma-Aldrich. And for immunostaining, Alexa Fluor 488 Phalloidin and DAPI were purchased from Invitrogen.

All chemicals were used as bought without any purification step and all the synthesis steps were performed using ultrapure water with a resistivity of 18.2MΩ.

2.2. Magnetic Nanoparticles Synthesis

The synthesis of the doped hydroxyapatite nanoparticles was achieved by chemical precipitation. Briefly, a calcium hydroxide $Ca(OH)_2$ solution (1.4818 g in 60 mL of H_2O) was prepared and kept under magnetic stirring overnight. This solution was heated up to 40°C in an oil bath and an influx of nitrogen was added to remove any dissolved oxygen and create an inert atmosphere system. After 5 minutes of nitrogen influx, $FeCl_2.4H_2O$ and $FeCl_3.6H_2O$ were simultaneously added to the solution as sources of Fe^{2+} and Fe^{3+} ions (0.376 g and 0.510 g, respectively).

The system was closed, and a phosphoric acid solution (0.892 ml in 20 ml of H_2O) was added dropwise at a rate of 0.500 mL/min using a peristaltic pump (ISMATEC-

ISM795C, Germany). The final solution was kept in suspension with constant stirring and heating. After one hour, the heating was interrupted, and the stirring maintained until the solution reached room temperature. Then, the stirring also ceased, and the solution was left at room temperature for 24 hours to age. After ageing, the nanoparticles were washed 3 times with ultra-pure water by centrifugation at 3500 rpm for 10 minutes and dried for 48 hours.

Finally, the dried powder was grinded in an agate mortar and pestle and sintered at 600°C for 1 hour in a sintering furnace (Termolab, Portugal) at a heating rate of 5°C/minute. The resultant powder was stored in a desiccator until further use.

2.3. $FeHap^{2+/3+}$ Nanoparticles Characterization

2.3.1. Size, Charge and Morphology

Dynamic light scattering (DLS) was used to measure the hydrodynamic diameter of the nanoparticles, while their surface charge was evaluated through zeta potential analysis. These measurements were performed at i3s (Porto), using a Zetasizer Nano ZS (Malvern, UK).

Briefly, 1 mg of $FeHap^{2+/3+}$ powder was added to 10 ml of ultrapure water and sonicated twice for 10 minutes using a Vibra-Cell™ probe sonicator (Sonics&Materials Inc., USA). Zeta potential was measured 3 times with a scattering angle of 173° and a He-Ne 633nm wavelength laser at 22°C.

To evaluate nanoparticles size and morphology, transmission electron microscopy (TEM) was used. This technique was performed at i3s (Porto), in a JEOL JEM-1400 electron microscope (JEOL Ltd., Japan), operating at an accelerating voltage of 80kV. Images were obtained using a CCD digital camera Orius 1100W (Gatan, USA) and analyzed with ImageJ® software (University of Wisconsin, USA).

For this analysis, a solution of 10 mg/ml of nanoparticles was prepared in ultrapure water and sonicated twice for 10 minutes (Vibra-Cell™, Sonics&Materials Inc., USA). Afterwards, 100 µL of this solution were added to 1 mL H_2O. From the diluted solution, a 10 µL drop was placed on a Formvar/carbon film-coated nickel mesh grid (Electron Microscopy Sciences, USA) and left to dry overnight.

2.3.2. Chemical Composition

The chemical composition of the nanoparticles was evaluated through Fourier-Transform Infrared Spectroscopy (FTIR) and Raman Spectroscopy (RAMAN).

FTIR was performed at i3s (Porto) using a Perkin-Elmer 2000 (Perkin-Elmer, USA) with a wavelength range 400–4000 cm^{-1} a $4cm^{-1}$ spectral resolution and the spectra resulted in an average of 64 scans. Approximately 2 mg of $FeHap^{2+/3+}$ powder was mixed with 200 mg of potassium bromide and compressed (8 Tons) in a hydraulic press (Grasedy Specac, UK) to obtain pellets for analysis.

RAMAN was performed at IFIMUP (Porto) in a Raman confocal spectrometer INVia^{TM} Qontor (Renishaw, UK) with a He-Ne laser of 514.5 nm wavelength and a spectral resolution of 0.15 cm^{-1}. For this analysis, a small amount of the ceramic nanoparticles was placed on a glass substrate and several grain regions were studied.

2.3.3. Crystallinity

Characterization of the nanoparticles crystalline phase was performed at IFIMUP (Porto) by X-ray Diffraction (XRD) using a Rigaku SmartLab diffractometer (Tokyo, Japan) within a 2θ range from 9° to 90° with a 0.02° step, using Cu source with a wavelength of λ=1.5406 Å, generated at 45kV and 200mA.

2.4. Hap Scaffold Fabrication

The porous hydroxyapatite scaffolds were produced using the sponge replica method. In brief, a polyurethane sponge (with density of 42 Kg/m3 and hardness of 3.4 kPa) was cut into 9x9x10 mm cubes and impregnated with a ceramic slurry containing nanohydroxyapatite microaggregates (g), distilled water (ml), and Dolapix CE64 (mL) as a dispersive agent in the ratio of 5:4.5:0.2, respectively.

The sponge cubes were immersed in the slurry and squeezed repeatedly to allow impregnation, then, the cubes were squeezed again with aluminum foil, to remove slurry in excess. The impregnated sponges were dried for approximately 30 minutes at 37°C in a laboratory oven before being subjected to a heat-treatment in a sintering

furnace. The heat-treatment consisted in a heating rate of 1°C/minute with 1 hour dwelling time at 600°C, followed by a heating rate of 4°C/minute until 1200°C and 3 hours plateau. The scaffolds were cooled to room temperature inside the furnace.

2.5. Hap Scaffold Characterization

2.5.1. Crystallinity

The presence of crystalline phases of the hydroxyapatite scaffolds after fabrication was evaluated through XRD, using the same parameters described in 2.2.3.

2.5.2. 3D Structure and Porosity

Analysis of the three-dimensional structure of the Hap Scaffolds was performed in i3s (Porto), using an X-ray micro-computed tomography (microCT) Skyscan 1276 scanner (SkyScan, Belgium).

The granules resulting from the breaking of a hap scaffold were immobilized inside a 0.2 mL Eppendorf and scanned for approximately 1h30min each, with a high-resolution mode of 0.99 µm and a pixel size of 3.99 µm. The energy and current of the X-ray source were 70 kV and 200 mA, respectively.

For reconstruction, processing and analysis, three SkyScan software were used. Reconstruction of the sliced image was achieved with NRecon (v.1.7.5.2). Using CTAn (v.1.19.3.1), around 500 slices were used to create a binary image, using a dynamic grey thresholding between 102 and 220, to distinguish ceramic material from pore voids. With the same software, the binary images were processed to analyze morphological parameters of interest. Illustrative images of the samples' cross sections were obtained with DataViewer (v.1.5.6.0).

2.6. Collagen Incorporation on Hap Scaffold

For collagen incorporation, type I collagen from bovine Achilles' tendon was swollen for 48h under magnetic stirring at 4°C in 0.01M HCL to achieve a 0.5% (w/v)

collagen solution. This solution was then homogenized for approximately 1h using an Ultra Turrax (T25 D, IKA®) at 10000 rpm.

From this concentrated solution, four solutions were prepared. Briefly, in 2 ml of 0.5% (w/v) collagen solution, 0, 5, 10 and 15 mg of $FeHap^{2+/3+}$ nanoparticles were added to obtain solutions with a collagen to nanoparticles mass ratio of 1/0, 1/0.5, 1/1 and 1/1.5. The solutions containing Nps were sonicated (Vibra-Cell™, Sonics&Materials Inc., USA) in cycles of 30 seconds until full dispersion of the nanoparticles (always in ice). After this step, the four solutions were diluted from 0.5% to 0.05% (w/v) of collagen.

These solutions were applied on the hydroxyapatite scaffolds dropwise, using approximately 160 µl in each scaffold (around 26 µl per face of the Hap cube). Then, to allow collagen inclusion, the scaffolds were kept in a vacuum oven (Binder, Germany) at room temperature for 48h.

Afterwards, collagen crosslinking was performed using a MES buffer solution (0.05M, pH=5.4), containing 0.83 g/L of NHS 2.3 g/L of EDC. The scaffolds were immersed in this solution for 2 h at 4 °C. Then, the solution was removed, and the scaffolds were washed for 30 min in MES buffer and twice for 30 min with ultrapure water. Finally, the scaffolds were dried for 24 h in a vacuum oven (Binder, Germany) and stored at room temperature.

After these steps, four types of Hap-COL-MNP scaffolds were obtained, differing in their magnetic nanoparticle content. From this point on, the samples will be referred to as 0MNP, 0.5MNP, 1MNP and 1.5MNP.

2.7. Hap-COL-MNP Scaffolds Characterization

2.7.1. Hap-COL-MNP Scaffolds Morphology

Scaffold morphology and collagen distribution within the scaffolds was observed by scanning electron microscopy, (SEM) and X-ray energy dispersive spectroscopy (EDS) was carried out for elemental analysis. This analysis was carried out in CEMUP (Porto) using a FEI Quanta 400 FEG ESEM/EDAX Genesis X4M. An acceleration voltage of 15 kV was used and secondary electron images were obtained. For that purpose, the samples

were fixed with epoxy resin (Araldite™) and sputter-coated with a palladium-gold alloy film for approximately 100 s (SPI Module Sputter Coater).

2.7.2. Mechanical tests

A compressive test was performed to estimate the fracture force and rupture profile of Hap and Hap-collagen scaffolds. This assay was performed on 5 replicas of each sample under the same conditions, at UCIBIO Requimte (Porto).

The analysis was carried out using a texture analyzer (Stable Micro Systems, TA-XT2i), with a load cell of 30 kg and a 4 mm stainless steel cylinder probe. The load was applied vertically, at a displacement rate of 0.1 mm/sec and covering 4 mm into the sample.

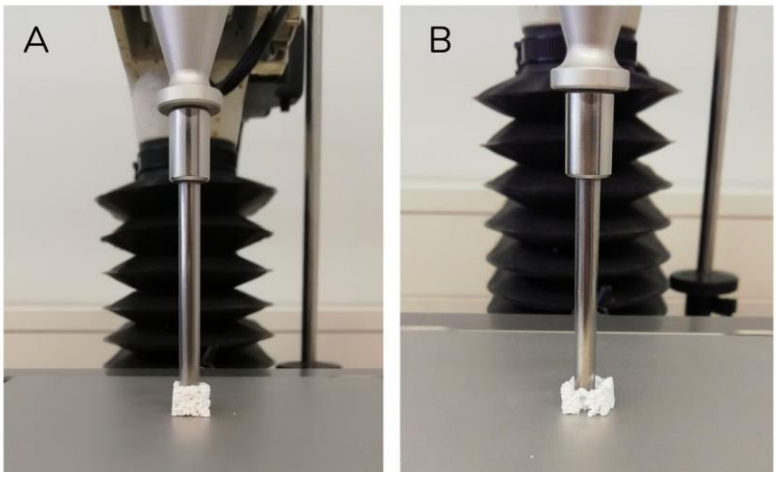

Figure 5. Representation of the compressive tests performed to Hap and Hap-COL scaffolds. (A) Initial contact between cylindrical probe and the sample. (B) Final placement of the probe at the end of penetration test in Hap-COL scaffold.

2.8. Apatite Deposition in Simulated Body Fluid

The apatite deposition on composites was evaluated according to Kokubo's method. Briefly, SBF was prepared by dissolving 8.035 g NaCl, 0.355 g $NaHCO_3$, 0.225 g KCl, 0.231 g $K_2 HPO_4 \cdot 3H_2O$, 0.311 g $MgCl_2 \cdot 6H_2O$, 39 ml HCl – 1.0 M, 0.292 g CaCl2, 0.072 g Na_2SO_4 and 6.118 g Tris in 1 L of distilled water. The solution was prepared in a plastic beaker and the reagents were added one by one to avoid apatite nucleation and

precipitation. The temperature of the solution was kept between 36°C and 37°C during the entire process and the final pH of the solution was adjusted to 7.4 with 1.0 M HCl.

All samples, 0MNP, 0.5MNP, 1MNP and 1.5MNP, were placed at the bottom of 50 mL falcons (with minimal contact between scaffolds and falcon walls), immersed in 50 mL of SBF and incubated at 37 °C for 7 and 21 days.

The apatite formation was evaluated by SEM as described in the section 3.4.1.

Figure 6. Representative image of the scaffolds position during immersion in simulated body fluid (SBF), showing that the scaffold surface had minimal contact with the falcon tube.

2.9. Biological Studies

2.9.1. Scaffold Preparation for Biological Studies

To investigate their effect on cell behavior, the four types of Hap-COL-MNP scaffolds (0MNP, 0.5MNP, 1MNP and 1.5MNP) were tested with and without the presence of an external SMF (samples subjected to static magnetic field, will be named 0MNP+SMF, 0.5MNP+SMF, 1MNP+SMF and 1.5MNP+SMF).

The static magnetic field was achieved by placing the culture plates on a permanent magnet (Super Magnetic plate 8x12 cm, OZ Biosciences, France).

On the day before cell seeding, the scaffolds were sterilized with 70% ethanol for 40 minutes, washed 3 times with PBS to remove any excess ethanol and left in complete medium overnight, to allow hydroxyapatite leaching and protein adsorption.

2.9.2. Cell Culture

MC3T3-E1 cells, an osteoblast precursor cell line, were cultured in alpha minimum essential medium (αMEM) supplemented with 10% fetal bovine serum and 1% penicillin/streptomycin under a humidified CO2 atmosphere at 37 °C. The medium was changed every other day and the cells were trypsinized with 0.25% trypsin (containing 1 mM EDTA) and split when reaching a confluence of 80%.

For the viability assay, cell were seeded in each scaffold at a concentration of $2x10^5$ cells/mL in αMEM supplemented with 10% fetal bovine serum, 1% penicillin/streptomycin and 1% fungizone (to be called α complete medium). Medium was changed every 3 days. Scaffolds without cells but incubated in the same media and environmental conditions were used as controls.

For the ALP staining and confocal microscopy, the same concentration of cells was seeded in each scaffold and the medium used was the above described α complete medium, supplemented with β-glycerophosphate, dexamethasone and ascorbic acid (to a final concentration of 10 mM, 10^{-8} M and $5x10^{-5}$ M, respectively). Medium was changed every two days.

2.9.3. Resazurin Assay

The metabolic activity of MC3T3-E1 cells was determined after 3, 7 and 10 days of cell culture, using the resazurin assay. The blue dye (non-fluorescent and non-toxic) is metabolized by the cells and converted to a pink, fluorescent dye.

On each timepoint, the medium was removed and replaced by α complete medium supplemented with 10% resazurin. After 3 hours, 200 µL of the resulting medium were transferred to a black 96-well plate and the fluorescence was measured at 550-605 nm in a microplate reader (SynergyMx, BioTek, VT) using Gen5 1.09 Data Analysis Software. The remaining medium was removed, scaffolds were washed twice with PBS 1x and fresh α complete medium was added.

2.9.4. ALP Staining

At 7, 14 and 21 days, cell medium was removed, and scaffolds were rinsed twice with PBS 1x and fixed using 3.7% paraformaldehyde for 15 minutes. All scaffolds were washed 3 times for 5 minutes with PBS and kept in PBS, in a 48 well plate, at 4°C until being processed.

For the ALP staining, 20 mg of Na-α-naphtyl phosphatase were added to 10 mL of Tris buffer (0.1 M, pH=10) and kept under magnetic stirring. After 10 minutes, 20 mg of fast blue RR salt were added, and the staining solution was stirred for more 10 minutes. Then, the resultant solution was filtered using a 0.22 µm syringe filter.

To each scaffold 450 µL of the staining solution were added and they were left in the dark for one hour at room temperature. Then, scaffolds were washed 3 times with distilled water and left to dry in air.

Finally, images of the staining were captured using Olympus SZX10 stereomicroscope and processed with ImageJ® software.

2.9.5. Immunostaining

For this purpose, scaffolds were prepared as described above (section 5.4.).

On the day before the analysis, PBS was removed and 450 µL of 0.2% Triton X-100 (in PBS) were added to permeabilize the cells for 10 min. After, cells were incubated for 30 min in 1% BSA solution in PBS.

Alexa Fluor 488 phalloidin was used, diluted in the BSA/PBS solution (1:100) to stain F-actin filaments, for 1 hour in the dark. Scaffolds were washed 3 times with PBS and incubated with DAPI (1:10 000 in PBS) for 10 minutes. Finally, the samples were washed 3 times with PBS.

Confocal images were acquired at i3s (Porto) using a Leica SP5 Confocal Microscope, using a 10x objective, and processed with ImageJ® software.

2.10. Statistical Analysis

Statistical analysis and graphs were carried out with the GraphPad Prism 5 software (GraphPad, USA). Data are represented as mean ± standard deviation (SD). Statistical analysis was performed using the analysis of variance one-way ANOVA, followed by a post hoc Tukey's test with a significance level of $p < 0.05$.

3. Results and Discussion

3.1. Characterization of Magnetic Nanoparticles

Iron doped hydroxyapatite has been widely studied as a less toxic substitute for magnetite SPIONS, which are, to this day, the most used MNPs for biomedical applications[85,86]. Many synthesis methods have been described, with different synthesis and sintering temperatures, using Fe^{2+}, Fe^{3+} or simultaneous inclusion of both iron phases[101].

They are mainly studied for bioimaging purposes, as well as for hyperthermia treatments with or without drug release[85,101]. They have also been referred for tissue regeneration, namely bone[94,102], hence their application in this research for a novel magnetic scaffold with bone regenerative properties.

3.1.1. Size, Charge and Morphology

Through TEM analysis (Figure 7) we were able to confirm that the synthetized MNPs present a heterogeneous needle-like morphology, with lengths varying from 20 to 70 nm and width of 5-13 nm. The images also show that the nanoparticles have a great tendency to agglomerate in aqueous suspension. This information is in agreement with the hydrodynamic size measured by DLS, of 588 ± 28.7 nm, which represents most probably the hydrodynamic size of an average Np aggregate, rather than a single nanoparticle.

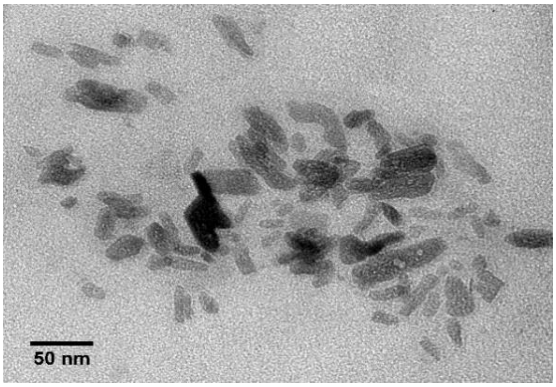

Figure 7. *Representative TEM image of the iron-doped (FeHap$^{2+/3+}$) nanoparticles.*

Colloidal stability is strongly dependent on electrostatic repulsions between surface charges[103], hence the minimum accepted zeta potential value to consider a colloidal suspension stable is 30 mV in modulus.

From the ELS, the measured zeta potential was -18.5 ± 0.3 mV, corresponding to a low surface charge. Therefore, it was expected that the magnetic nanoparticles in solution would not have an ideal behavior and would form aggregates.

This aspect could be easily overcome by adding a surface modification step after nanoparticle synthesis. SPIONS for example, are usually coated with hydrophilic molecules, such as silicon, dextran, citrate, PVA, PEG, among others, to enhance their stability in solution and decrease opsonization when administered intravenously[85]. Though, in our work, it was not considered necessary to perform these modifications, since the nanoparticles will be included in the fabrication of a 3D scaffold and not in circulation.

3.1.2. Chemical Composition

As described earlier, hydroxyapatite is an orthophosphate, therefore, it presents calcium, phosphate and hydroxyl groups in its chemical composition. The presence of such functional groups can be identified by FTIR analysis.

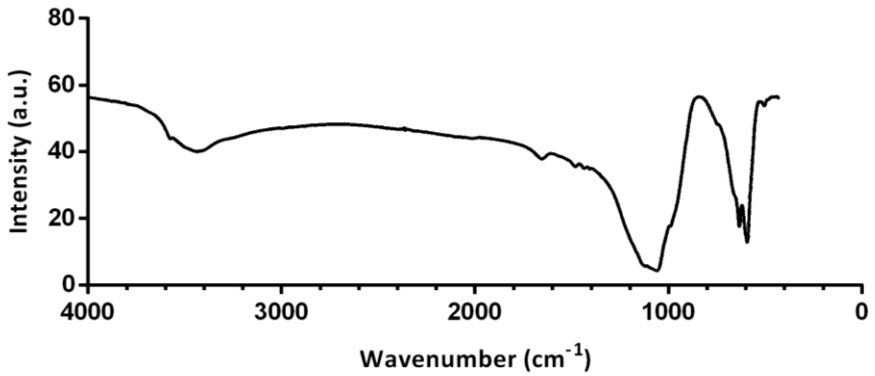

Figure 8. Fourier transform infrared spectra of the iron-doped ($FeHap^{2+/3+}$) nanoparticles. Vertical offset was adjusted.

The FTIR spectrum presents a short peak at ~3570 cm^{-1}, associated with O-H stretching vibrations of the hydroxyapatite lattice[104]. The band at ~3430 cm^{-1} and the peak at ~1638 cm^{-1} correspond to water. The small peaks between 1460 and 1380 are related to residual carbonates (C-O), possibly atmospheric CO_2 adsorbed to the Hap lattice[105].

Finally, all four vibrational modes of PO_4^{3-} are shown in the spectra. A small peak of v1 mode appears at ~961 cm^{-1}, v2 is shown at ~473 cm^{-1}, the peaks at ~1097 and ~1035 cm^{-1} represent v3, and v4, with the easily detected peaks at ~567 and ~610 cm^{-1} [105].

According to the literature, the spectrum shows all the bands associated with Hap. The substitution of calcium with iron is only visible through comparison with a pure hydroxyapatite spectrum, since it provokes shifts in wave number and transmittance of PO_4^{3-} and OH^- [93]. The broadening of the peaks is another reported difference in FTIR spectrum of iron doped hydroxyapatite when compared to the spectrum of the pure material[93]. This last aspect is well visible in the spectrum presented in Figure 8.

In the Raman spectra (Figure 9), the presence of all vibrational modes of phosphate was also confirmed. The highest intensity peak at ~956 cm^{-1}, characteristic of Hap spectrum, corresponds to the symmetrical stretching mode (v1) of PO_4^{3-}.

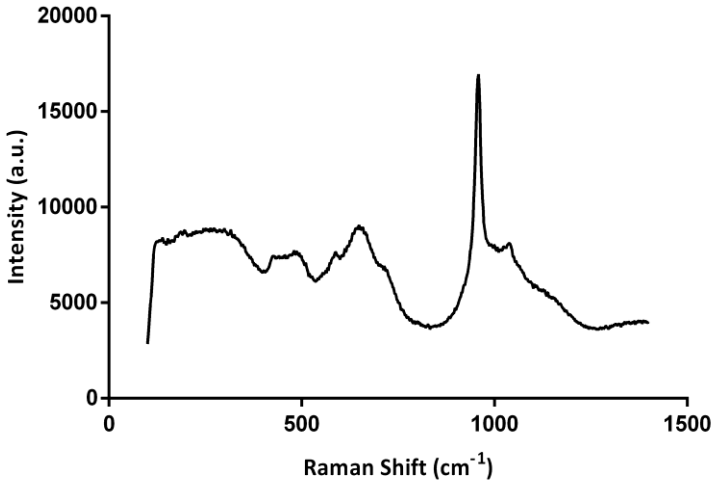

Figure 9. Raman spectra of the iron-doped ($FeHap^{2+/3+}$) nanoparticles. Vertical offset was adjusted.

With smaller peaks vibrational modes 2, 3 and 4 can also be found in the spectra. At ~429 and ~490 cm^{-1} vibrational mode 2 (v2), v4 is represented at ~659 and -591 cm^{-1}, and v3 at ~1043 cm^{-1}[106]. No iron related peaks were observed in the RAMAN spectra.

3.1.3. Crystallinity

XRD analysis was used to assess the effects of iron incorporation in the lattice of Hap on the crystalline structure of the material, as well as to see if any secondary phases were formed during the synthesis process.

The wide bands shown in the diffractogram (Figure 10) suggest that the inclusion of iron in the Hap lattice, combined with the low sintering temperature (600 °C) resulted in an amorphous apatite structure. Despite the low crystallinity, almost all the peaks present in the diffractogram are characteristic of hydroxyapatite (obvious by observation of the overlapped diffractograms), besides one small peak at 2θ=~31°, which relates to the secondary phase β-TCP (marked in the figure), commonly found in these nanoparticles, produced by wet chemical precipitation[86,107].

Iron related peaks are not visible in the diffractogram, these have been reported to appear at 2θ=36°[86], overlapping with an Hap peak, present in the same position.

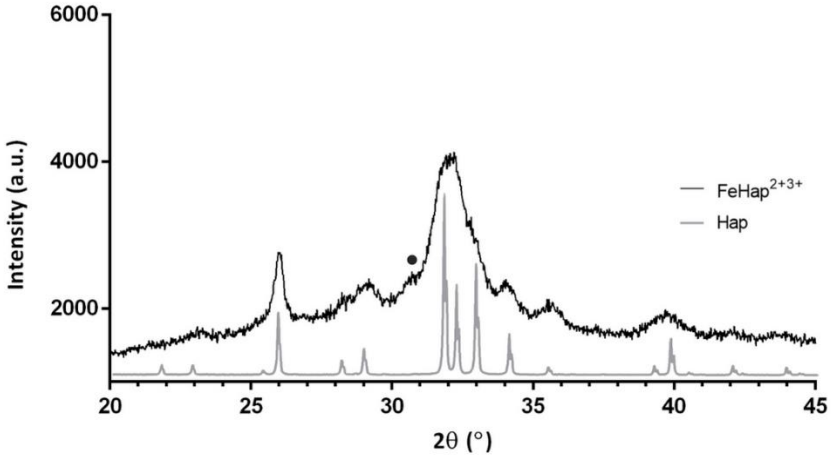

Figure 10. XRD diffractogram of iron-doped ($FeHap^{2+/3+}$) nanoparticles. The black dot marks a peak corresponding to a β-TCP phase. Vertical offset was adjusted.

3.1.4. Magnetic Behavior

Regarding the magnetic behavior of the nanoparticles, in Figure 11 we can observe a sequence of images of FeHap$^{2+/3+}$ nanoparticles in solution being attracted to a magnet (B to D), as well as sinking to the bottom of the recipient when the magnet is removed. This observation allows us to conclude that the nanoparticles can be manipulated by external magnetic fields.

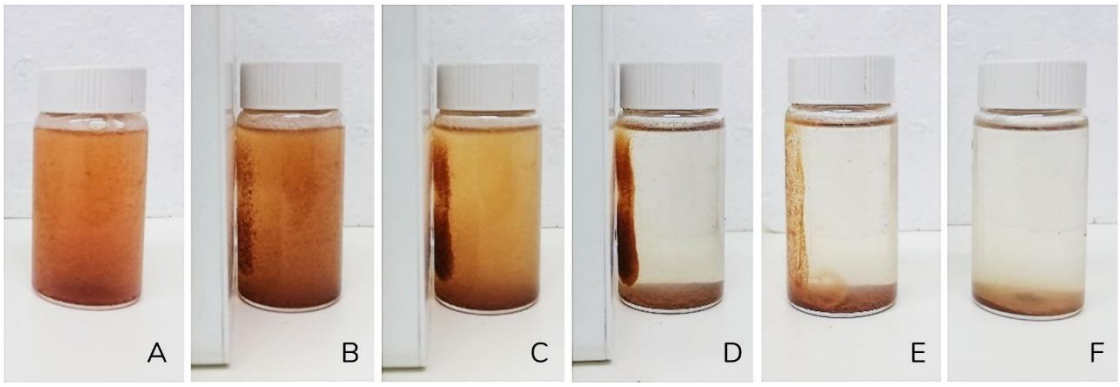

Figure 11. Magnetic attraction of iron-doped (FeHap$^{2+/3+}$) nanoparticles. (A) Nps in water suspension, (B-D) Nps being atracted to an external magnet, (E-F) Nps sinking when magnet is removed.

3.2. Characterization of Hap Scaffold

A scaffold for bone regeneration, should be osteoinductive, osteoconductive and capable of promoting osteogenesis. Also, the scaffolds should have a degradation rate that accompanies the new bone formation.

Before opting to proceed with the Hap slurry described in the methods section, that had been previously optimized for producing scaffolds by sponge impregnation[107,108], different BCP scaffolds were produced, varying in their percentage of β-TCP (10, 15, 20 and 30% of the ceramic part of the slurry).

The blend between a more stable phosphate phase, Hap, and a more soluble one, β-TCP, allows for faster degradation of the scaffold, while promoting new bone ingrowth[45], hence the increased interest in this tunable material.

However, despite the attempts with different TCP percentages and distinct sintering cycles, the resultant BCP scaffolds presented poor mechanical properties after sintering and were hard to maneuver without breaking.

Research groups that have described the incorporation of β-TCP in porous ceramic scaffolds have used different fabrication methods, such as template casting[109], selective laser sintering[110], 3D-printing[45], among others. In our case, the slurry composition may need to be optimized in order to include β-TCP in porous scaffolds by sponge impregnation.

3.2.1. Crystallinity

The hydroxyapatite scaffolds, sintered at 1200 °C for 3h, were ground to powder and analyzed by X-ray diffraction to verify the purity and crystallinity of the resultant product.

The hydroxyapatite suffered no phase transformation during the sintering process, instead, the diffractogram (Figure 12) shows a highly crystalline and pure Hap phase, with no peaks corresponding to TCP phases (all present peaks correspond to Hap characteristic peaks). This confirms the high thermal stability of the initial nano-Hap powder.

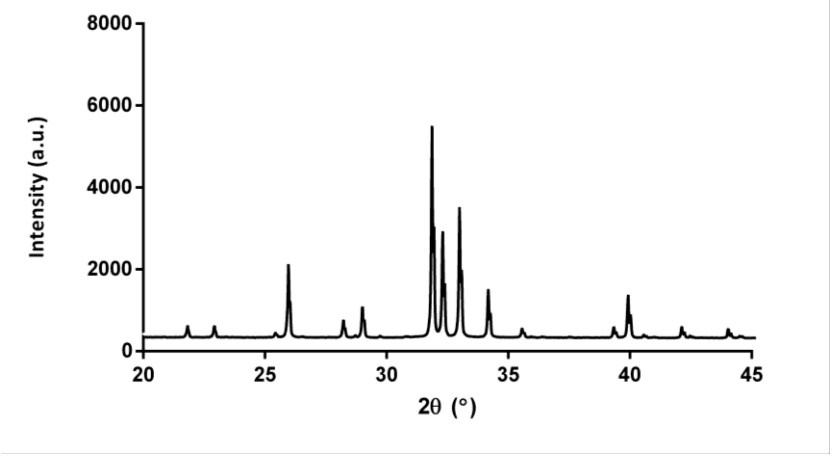

Figure 12. XRD diffractogram of hydroxyapatite (Hap) scaffold. All peaks correspond to hydroxyapatite. Vertical offset was adjusted.

3.2.2. 3D Structure and Porosity

Micro CT analysis was performed to achieve a better understanding on the Hap scaffolds 3D structure, as well to determine aspects such as percentage of porosity and mean pore size. This technique allows for a non-destructive evaluation of samples, with 3D image reconstruction and several quantitative measurements.

In this case, the scaffold presented 70,8 % (± 0,42 %) interconnected porosity and a mean macropore size of 348 µm (± 80 µm), which is within the values considered optimal for the fabrication of an osteoconductive scaffold for bone regeneration. It has been said that such material should have 60-80% porosity (similarly to trabecular bone) and a macropore size ranging from 150-500 µm[55], to allow for cell migration and new bone formation inside the material's matrix.

Micro and nano porosity are also important for angiogenesis during bone formation, though these cannot be accessed by micro-CT.

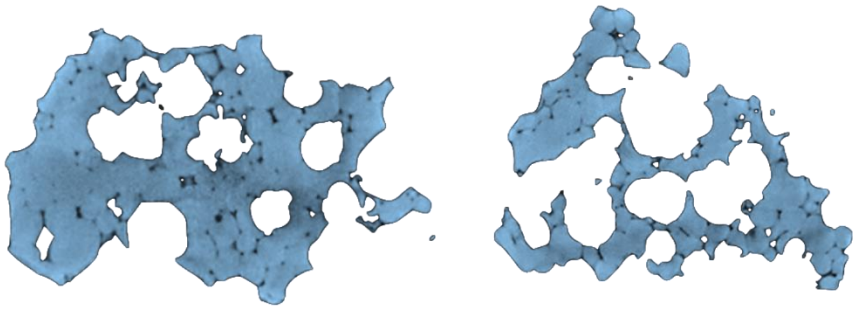

Figure 13. Representative slice images of hydroxyapatite scaffold acquired by Micro-CT.

3.3. Characterization Hap-COL Scaffold

3.3.1. Hap-COL Scaffolds Morphology

Scaffolds were analyzed by SEM and the acquired images provide a better understanding on the collagen distribution inside the scaffold. In Figure 14 is possible to observe that collagen forms a layer on top of the hydroxyapatite grain (C and D), as well as larger fibers and nets across macropores (B). We can also see the collagen lining pore walls, in a thin layer (A).

All images presented in Figure 14 belong to scaffolds without nanoparticles (0MNP), however, collagen with nanoparticles is similarly distributed onto the respective scaffolds (0.5MNP, 1MNP and 1.5MNP).

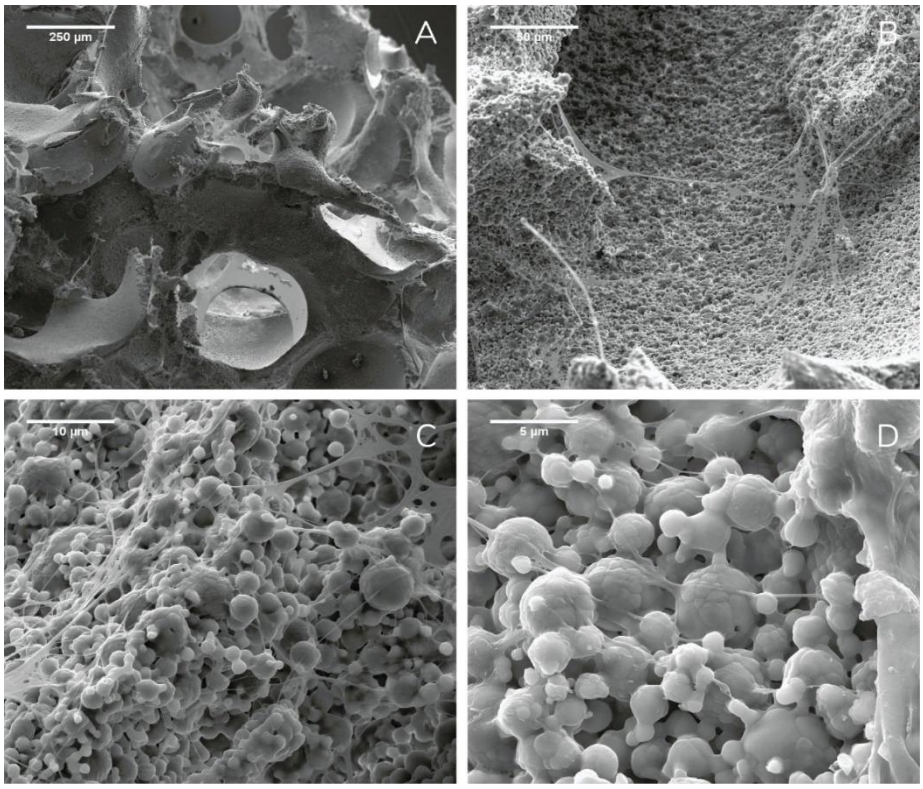

Figure 14. Representative SEM images of collagen distribution inside the scaffolds. The four images correspond to the sample 0MNP. (A) Collagen films riming the scaffolds macropores, scale 250 µm. (B) Collagen distribution in a fiber-like structure onto the scaffolds, scale 50 µm. (C-D) Collagen layer covering hydroxyapatite grains and connective collagen fiber-like structures, scale 10 and 5 µm, respectively.

The presence of nanoparticles incorporated in the collagen matrix has only visible effects on the collagen texture, increasing its roughness. As seen in Figure 15, small aggregates of nanoparticles are embedded in the collagen matrix, making a denser, rougher structure as the concentration of nanoparticles rises, from 0.5MNP (A), to 1MNP (B) and finally 1.5MNP (C).

EDS analysis was also performed in these scaffolds to confirm the composition of the observed aggregates. Spectra D represents zones where no nanoparticles are seen (although they can be present in a layer bellow the image focus point, hence the small appearance of iron in areas where aggregates are not visible), while spectra E represents zones with visible nanoparticles aggregates (marked with arrows along the images). In spectra E the iron peaks are more evident, hence confirming the presence of the iron-doped nanoparticles.

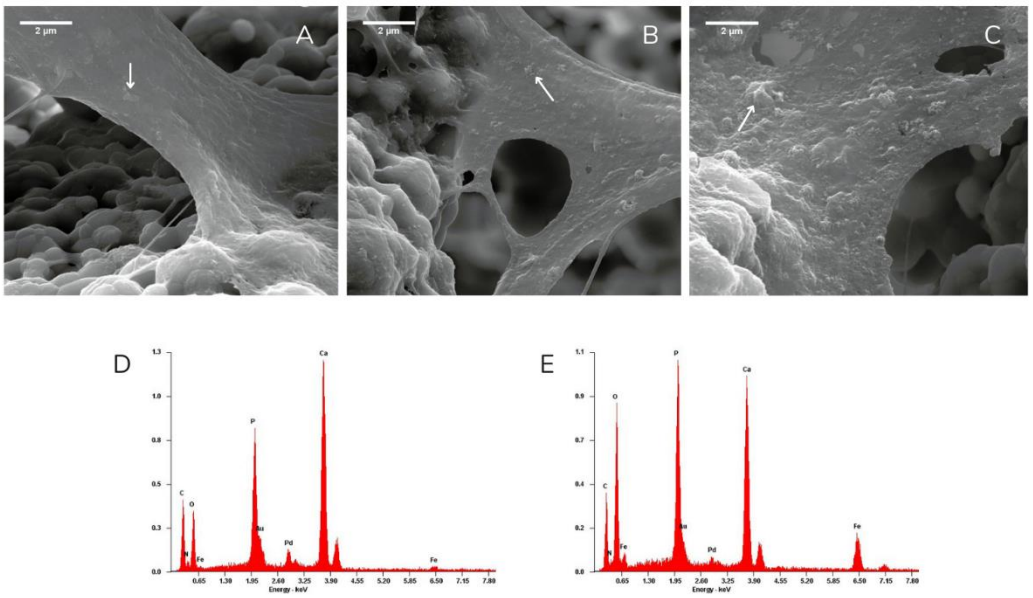

Figure 15. Representative SEM images of FeHap$^{2+/3+}$ nanoparticles in the collagen films on samples (A) 0.5MNP; (B) 1MNP; (C) 1.5MNP, Scale 2 µm. (D) EDS analysis of collagen zones. (E) EDS analysis of nanoparticles aggregates in the collagen (example marked with an arrow in each sample).

3.3.2. Mechanical Test

The mechanical properties of porous ceramic structures are not easy to access, especially in highly heterogeneous samples. The pore patterns verified in these materials can be random or designed, depending on the chosen fabrication method.

A designed porosity can only be achieved with an additive manufacturing method, and these materials will have highly comparable mechanical and structural properties between samples. When porous scaffolds are produced resorting to foam templates, polymer microbeads or foaming agents, they will exhibit random porosity, meaning that the pore distribution throughout the material will not follow any long-range order or alignment[111].

With sponge replica, for example, defects in the original PU sponge, as well as the natural structural heterogeneity, lead to the fabrication of unequal samples with random porosity. Therefore, there was considerable variation observed in the mechanical response between scaffolds.

Concerning the maximum calculated compression strengths calculated, for Hap scaffolds was 1,14 MPa (± 0,6) and for the samples containing hydroxyapatite and collagen (between 0MNP, 0.5MNP, 1MNP and 1.5 MNP no significative differences were found) was 1,25 MPa (± 0,6). The reported strength range of trabecular bone varies between 1 and 10 MPa[111], therefore, a bone substitute for this end should perform similarly.

Despite the similarity between the two values presented, the stress-strain profiles of samples with and without collagen are visibly different. In Figure 16 are shown two representative stress-strain curves of hydroxyapatite and hydroxyapatite-collagen scaffolds. It is possible to see that the Hap sample fractured completely at its maximum compression strength while the samples containing collagen had multiple fractures.

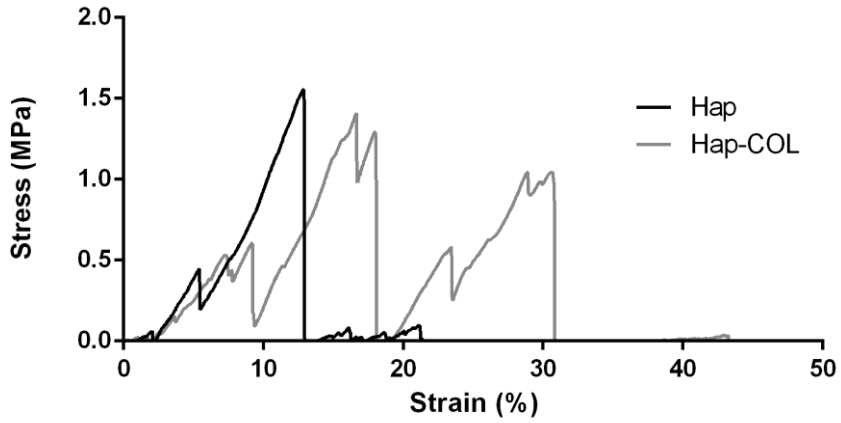

Figure 16. Representative Stress-Strain curves of Hap and Hap-COL Scaffolds during compression test. Stress was calculated dividing the force (N) values, obtained during the analysis, by the cross-sectional area of the samples.

We also observed during the assays, that when Hap scaffolds reached their maximum strength, they completely shattered and some fragments were projected, while the Hap-COL ones stayed in place, surrounding the testing probe (visible in section 2.7.2, Figure 5-B). It was clear that the collagen fibers were supporting the Hap fragments, even after rupture, which is an interest behavior for a material to be implanted in a high load area.

3.4. Apatite Deposition in SBF

Biomaterial's immersion in simulated body fluid is a well-established method of evaluating its potential for bone tissue regeneration purposes. Normally, after immersion for several days or weeks, the samples are analyzed by SEM to confirm if there is evident apatite formation on the materials.

The presence of an apatite layer on top of the material, formed in these conditions (SBF), strongly suggests that in a biological environment, the material can also promote the formation of this layer, hence being able to bond to the surrounding bone[112].

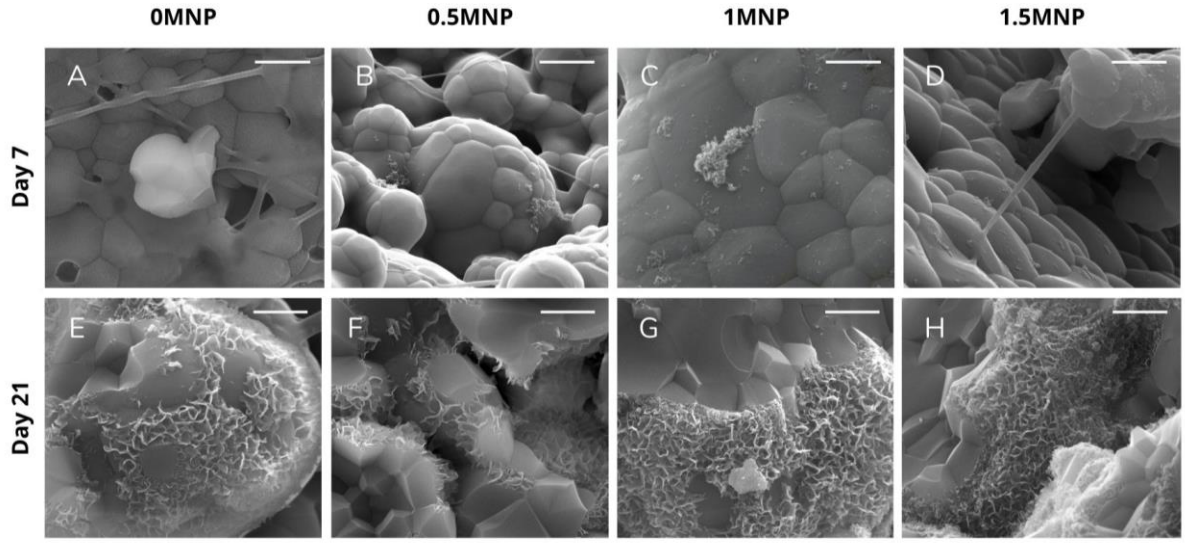

Figure 17. Representative SEM images of the scaffolds after immersion in simulated body fluid (SBF) for 7 (A-D) and 21 (E-H) days. (A,E) 0MNP; (B,F) 0.5MNP; (C,G) 1MNP; (D,H) 1.5MNP. Scale bar: 1 µm.

The morphology of the scaffolds after 7 (A-D) and 21 (E-H) days is revealed in Figure 17. After one week (day 7) of immersion in SBF, there was no apparent apatite formation on the scaffold's surface. The scaffold 0MNP (A) shows a smooth texture, as it did before this assay. In the scaffolds containing nanoparticles it is possible to see small structures on the scaffold surface, however, these are probably nanoparticles aggregates visible in the collagen matrix as shown in section 3.3.1 (Figure 15).

After 21 days in SBF, on the other hand, petal-like apatite was found in all four scaffolds, with no evident differences between the newly formed structures in the

different materials. We can assume by these results that the nanoparticles embedded in the collagen matrix have no effect on the intrinsic ability of the material to form bone-like apatite.

3.5. Biological Studies

3.5.1. Resazurin Assay

The resazurin assay was used to assess differences in the metabolic activity of pre-osteoblastic cells when cultured in the different scaffolds, with and without magnetic stimulation. The fluorescent product that results from the reduction of the blue dye is measured, and its intensity can be correlated with the number of viable, metabolically active cells[56].

Cells cultured in 0MNP had the same behavior when cultured with and without magnetic stimulation at all timepoints. Meaning that the intensity of the magnetic field used in this experiment, alone, has no effects on the proliferation of MC3T3-E1 cells, which is in concordance with previous studies[113].

Regarding the same sample, 0MNP, statistically significant differences were found in cultures without magnetic stimulation when compared to 1MNP and 1.5MNP at day 7 ($p < 0.05$ and $p < 0.001$, respectively), and 0.5MNP, 1MNP and 1.5MNP at day 10 ($p < 0.001$, $p < 0.01$ and $p < 0.0001$, respectively). From this we can conclude that the presence of $FeHap^{2+/3+}$ nanoparticles in the collagen matrix coating the scaffolds has positive effects on osteoblast proliferation and viability, even at the lowest concentration.

With SMF, the differences in cell metabolic activity between all three samples with nanoparticles (0.5MNP, 1MNP and 1.5MNP) and the control (0MNP) were observed from day 3, to day 10 with $p < 0.0001$ (detailed information found in supplementary material).

In the graph (Figure 18) are marked the differences found at day 3 between each sample with MNP and their counterpart with SMF. At day 7, this difference is only statistically significant for sample 1.5MNP and as of day 10, none was found.

Nonetheless, the tendency is maintained along the timepoints, for which we can assume that in terms of metabolic activity of MC3T3-E2 cells, the combination of static magnetic field and magnetic nanoparticles, results in a synergic effect, enhancing it.

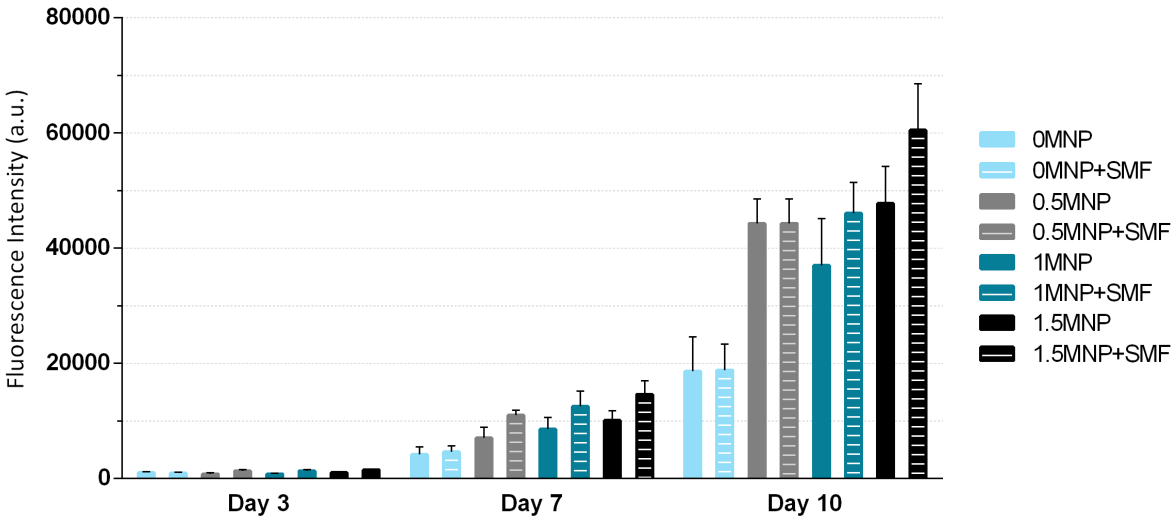

Figure 18. Results obtained from Resazurin/ AlamarBlue assay at 3, 7 and 10 days of culture, with and without the influence of a static magnetic field (SMF). Error bars represent the standard deviation. Statistically significant differences are marked with * ($p < 0.05$), ** ($p < 0.01$), *** ($p < 0.001$) or **** ($p < 0.0001$)

3.5.2. ALP Staining

During the early stages of new bone matrix mineralization, alkaline phosphatase enzyme is secreted by active osteoblasts. The level of ALP expression is correlated with osteoblast differentiation, as well as, synthesis and mineralization of extracellular matrix, being an important biomarker for osteogenesis[114].

To qualitatively assess the ALP activity of MC3T3-E1 cells cultured with osteogenic medium, scaffolds from all conditions (0MNP, 0.5MNP, 1MNP and 1.5MNP, with and without the influence of a SMF) were stained after 7, 14 and 21 days of culture, with a solution of sodium α-naphthyl phosphate and fast blue RR salt, as previously described[115]. With this method, ALP is marked in a color range from brown to black, where black precipitate represents higher ALP activity. The staining was performed in one scaffold per condition and the results are shown in Figure 19.

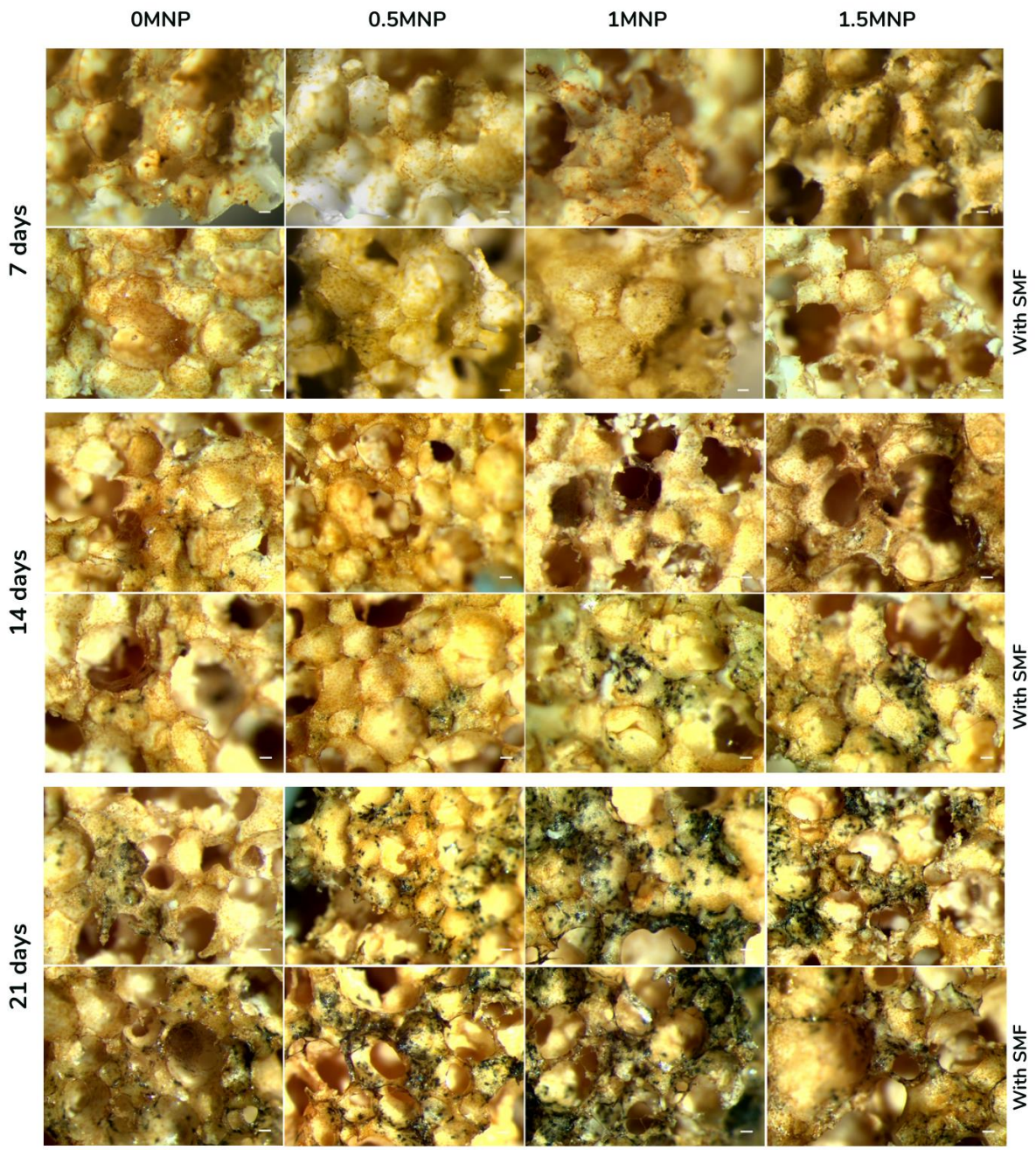

Figure 19. Representative images of ALP staining with Na-α-naphthyl phosphate and fast blue RR salt in scaffolds cultured with MC3T3-E1 cells in osteogenic medium with and without the influence of an external static magnetic field. The staining ranges from brown to black representing lower to higher ALP activity, respectively. Scale bar: 100 µm.

At day 7 is possible to see that all samples present mainly brown precipitates, indicating that ALP is already active at this timepoint. Some black precipitates are shown in the samples 1.5MNP without SMF and in 0.5MNP and 1MNP with static magnetic field, however, they are not highly significant to represent actual differences in ALP activity between samples.

At day 14, however, we can see that the images from the scaffolds made solely of hydroxyapatite and collagen (without magnetic nanoparticles), 0MNP, are very similar with and without the presence of a SMF, showing that, in this material, the magnetic field has no influence in ALP activity, therefore, no influence in cell differentiation. This result correlated with the measured metabolic activity of the cells, which was found to be equal in these two samples at day 10.

As for all three samples containing MNPs, at this timepoint, we can easily detect that the conditions with SMF present more black precipitates than their equivalents cultured without SMF. This suggests that the added magnetic field had a positive influence in ALP secretion and therefore, osteoblastic differentiation and matrix mineralization.

When observing the images from day 21, it is evident at this timepoint that the scaffolds containing magnetic nanoparticles led to higher cell differentiation than the scaffold without MNPs, since the first ones present many more black granules.

However, the influence of the static magnetic field is not evident at day 21. All four samples show similar patterns of brown and black when compared to their equivalents cultured with static magnetic field. Finally, it seems that the sample 1MNP leads to higher ALP activity at day 21, when compared to the sample with higher nanoparticle content, 1.5MNP, thought quantitative studies should be done to access these differences more effectively.

3.5.3. Immunostaining

Osteoblast behavior and adopted morphology when in interaction with a new surface is highly important when proposing a novel biomaterial for bone regeneration. The distribution of MC3T3-E1 cells cultured in 0MNP and 1.5MNP scaffolds with and without magnetic stimulation were accessed after 7 and 21 days of culture by labeling the actin cytoskeleton (green) and the nucleus (blue) and acquiring fluorescence images.

The images presented in Figure 20 suggest that, at day 7 (A-D), the SMF has an inhibition effect on cell proliferation. This is not in agreement with the results from the

resazurin assay, however, this previous assay was performed with growing medium, without differentiation factors.

A different study had already reported a reduction in the proliferation of another pre-osteoblastic cell line at day 7 when exposed to SMF. The group tested the cultures for the stress marker Lactate Dehydrogenase (LDH), and found no differences between the cultures with and without SMF, therefore concluding that the observed inhibition was not due to cellular apoptosis, stress or disruption of membrane integrity[96].

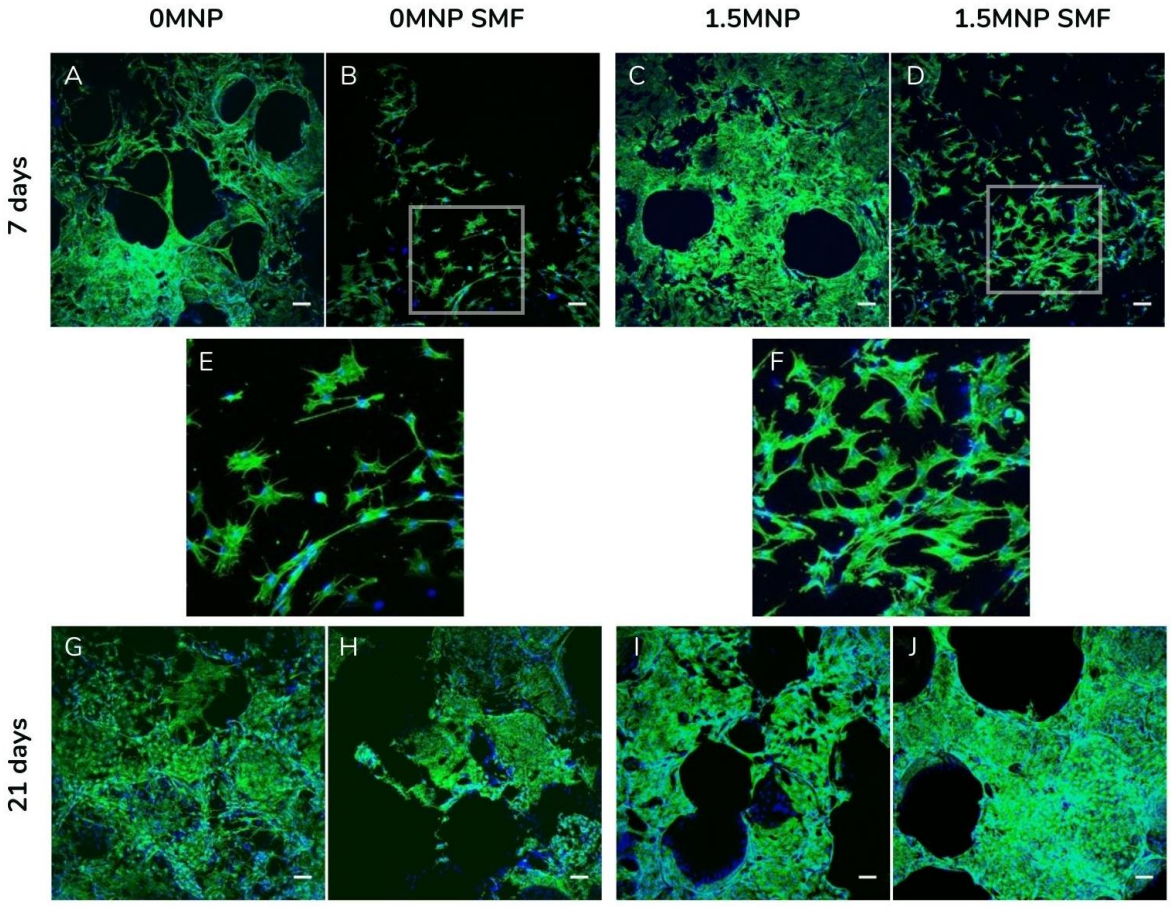

Figure 20. Confocal Z-stack images of actin (green) and nucleus (blue) of MC3T3-E1 cell cultured for 7 (A-F) and 21 (G-J) days in 0MNP and 1.5MNP scaffolds with and without the influence of a static magnetic field (0MNP SMF, 1.5MNP SMF). (E) and (F) are amplified images of the selected areas in (B) and (D), respectively.

A more recent study carried by Bolin Tang and his team found, when testing magnetic nanocomposite coatings, that the external influence of a static magnetic field enhanced MC3T3-E2 cell proliferation up to day 4, but seemed to cause a decrease at

day 7 [116]. They attributed this to a partial differentiation of the cells at day 7 when subjected to the SMF.

Having these results in mind, we are attributing the apparent decrease in cell proliferation with SMF at day 7 to an early start in the differentiation process of cells, when cultured with differentiation factors and exposed to the static magnetic field. Moreover, it is possible to see by the magnifications shown in Figure 20 (E and F) that cells exhibit a dendritic shape with cytoplasm projections and connections between neighbor cells. Furthermore, even with this inhibition in both samples, it seems that the sample with magnetic nanoparticles (1.5MNP+SMF, Figure 20-D) lead to higher cellular proliferation.

Day 7 images of scaffolds without SMF and day 21 images of all samples show that the cells are uniformly adhered along the curved pore walls of the scaffolds. Both images of samples containing magnetic nanoparticles, 1.5MNP (I and J), at day 21 seem to present a denser cell layer, when compared to samples without MNPs (G and H). Between samples 1.5MNP (I) and 1.5MNP+SMF (J) at day 21, the last seems to have resulted in an even denser cell layer, hence, the higher cell proliferation observer at day 21 was when the magnetic scaffold was combined with the static magnetic field.

(page intentionally left blank)

4. Conclusions and Future Perspectives

In this work, a novel magnetically responsive scaffold composed of hydroxyapatite and coated with collagen and iron doped hydroxyapatite was developed and characterized. Preliminary biological studies were also performed to confirm its potential as an implantable bone regenerative biomaterial.

The synthesis method applied in the fabrication of the $FeHap^{2+/3+}$ nanoparticles for this work had already been optimized, therefore, most of the results obtained during the characterization process were expected. Nano rods with lengths between 20 and 70 nm were produced and chemical analysis revealed that the nanoparticles were indeed hydroxyapatite, though with an amorphous structure, due to the inclusion of iron in the Hap lattice. The magnetization properties of the nanoparticles were not possible to assess for the aim of this research. In future works, analysis using a superconducting quantum interference device (SQUID) should be performed, for the nanoparticles, as well as for the scaffolds containing nanoparticles (0.5MNP,1MNP and 1.5MNP), to understand the effect of the different percentages of nanoparticles on the total magnetization of the material.

The hydroxyapatite scaffolds were also produced invoking a previously described method and parameters such as porosity, mechanical strength and ability to form an apatite layer were evaluated and found adequate for a scaffold for bone regeneration. The collagen incorporation onto the porous scaffolds was successful, though a refinement to the process could be the better dispersion of the nanoparticles in the collagen matrix. Nonetheless, the resultant roughness of the collagen didn't seem to provoke any negative effects on the mechanical properties of the final construct, nor on cell behavior.

Through biological studies with MC3T3-E1 pre-osteoblastic cells, the novel scaffold revealed to be promising for bone regeneration purposes. The surface of the material promoted cell adhesion, the interconnected porosity allowed for cell migration, and cells presented a good morphology when cultured onto the scaffold. The inclusion of nanoparticles in the collagen coating enhanced cell proliferation and seemed to

promote osteoblastic differentiation. Further tests should be performed in order to confirm this, starting with ALP quantification. This was attempted during this thesis, following previous protocols that described the possibility of lysing the cell membranes without previously detaching them from the scaffold, however, we were not successful with this method. In future work the detachment of cells from the scaffold should be attempted in order to have isolated cells to lyse and retrieve its contents to use in quantifications such as ALP, total protein end even DNA. Through DNA analysis it would be possible to quantify the expression of osteogenic markers such as ALP, COL-I, OCN and OPN, which would result in a more robust set of results to validate our theory.

Another important conclusion relates to the influence of the external magnetic field used during biological studies, which seemed to act in synergy with the magnetic scaffolds in terms of proliferation and differentiation. Unfortunately, we were not able to access the intensity of the magnetic field produced by the permanent magnet used in the experiments, which would be important to better correlate our findings with previously described ones in the literature.

Finally, a similar scaffold, without the nanoparticle content, has been developed in our research group, with the ability to release vancomycin, allowing for infection control on the implant site. Therefore, the inclusion of vancomycin or a different interest molecule in the collagen coating, combined with the nanoparticles could result in a more complete scaffold for bone regeneration.

5. References

1. Walsh, M. C. *et al.* Osteoimmunology: Interplay between the immune system and bone metabolism. *Annu. Rev. Immunol.* **24**, 33–63 (2006). doi.10.1146/annurev.immunol.24.021605.090646.

2. Lopes, D., Martins-Cruz, C., Oliveira, M. B. & Mano, J. F. Bone physiology as inspiration for tissue regenerative therapies. *Biomaterials* **185**, 240–275 (2018). doi.10.1016/j.biomaterials.2018.09.028.

3. Ginebra, M. P., Espanol, M., Maazouz, Y., Bergez, V. & Pastorino, D. Bioceramics and bone healing. *EFORT Open Rev.* **3**, 173–183 (2018). doi.10.1302/2058-5241.3.170056.

4. Alexey Kashpersky. Official website - Bone Cross Section. https://kashpersky.com/bone-cross-section-for-radius-digital-science.

5. Vielreicher, M., Bozec, A., Schett, G. & Friedrich, O. Murine Metatarsus Bone and Joint Collagen-I Fiber Morphologies and Networks Studied With SHG Multiphoton Imaging. *Front. Bioeng. Biotechnol.* **0**, 455 (2021). doi.10.3389/FBIOE.2021.608383.

6. Salgado, A. J., Coutinho, O. P. & Reis, R. L. Bone tissue engineering: State of the art and future trends. *Macromol. Biosci.* **4**, 743–765 (2004). doi.10.1002/mabi.200400026.

7. Kenkre, J. S. & Bassett, J. H. D. The bone remodelling cycle. *Ann. Clin. Biochem.* **55**, 308–327 (2018). doi.10.1177/0004563218759371.

8. Taton, T. A. Boning up on biology. *Nature* **412**, 491–492 (2001). doi.10.1038/35087687.

9. Zhu, G. *et al.* Bone physiological microenvironment and healing mechanism: Basis for future bone-tissue engineering scaffolds. *Bioact. Mater.* **6**, 4110–4140 (2021). doi.10.1016/j.bioactmat.2021.03.043.

10. Peng, J. *et al.* Magnetic Materials in Promoting Bone Regeneration. *Front. Mater.* **6**, 1–14 (2019). doi.10.3389/fmats.2019.00268.

11. Georgess, D., Machuca-Gayet, I., Blangy, A. & Jurdic, P. Podosome organization drives osteoclast-mediated bone resorption. *Cell Adhes. Migr.* **8**, 192–204 (2014). doi.10.4161/cam.27840.

12. Fernandez-Yague, M. A. *et al.* Biomimetic approaches in bone tissue engineering: Integrating biological and physicomechanical strategies. *Adv. Drug Deliv. Rev.* **84**, 1–29 (2015). doi.10.1016/j.addr.2014.09.005.

13. Oryan, A., Alidadi, S., Moshiri, A. & Maffulli, N. Bone regenerative medicine: Classic options, novel strategies, and future directions. *J. Orthop. Surg. Res.* **9**, 1–27 (2014). doi.10.1186/1749-799X-9-18.

14. Hutmacher, D. W. Scaffolds in tissue engineering bone and cartilage. *Biomater. Silver Jubil. Compend.* **21**, 175–189 (2000). doi.10.1016/B978-008045154-1.50021-6.

15. Winkler, T., Sass, F. A., Duda, G. N. & Schmidt-Bleek, K. A review of biomaterials in bone defect healing, remaining shortcomings and future opportunities for bone tissue engineering: The unsolved challenge. *Bone Jt. Res.* **7**, 232–243 (2018). doi.10.1302/2046-3758.73.BJR-2017-0270.R1.

16. Ehrler, D. M. & Vaccaro, A. R. The use of allograft bone in lumbar spine surgery. *Clin. Orthop. Relat. Res.* 38–45 (2000) doi:10.1097/00003086-200002000-00005. doi.10.1097/00003086-200002000-00005.

17. Citardi, M. J. & Friedman, C. D. Nonvascularized autogenous bone grafts for craniofacial skeletal augmentation and replacement. *Otolaryngol. Clin. North Am.* **27**, 891—910 (1994).

18. Brydone, A. S., Meek, D. & MacLaine, S. Bone grafting, orthopaedic biomaterials, and the clinical need for bone engineering. *Proc. Inst. Mech. Eng. Part H J. Eng. Med.* **224**, 1329–1343 (2010). doi.10.1243/09544119JEIM770.

19. Oryan, A., Moshiri, A. & Sharifi, P. Advances in injured tendon engineering with emphasis on the role of collagen implants. *Hard Tissue* **1**, (2012). doi.10.13172/2050-2303-1-2-292.

20. Nandini, Vv., Venkatesh, Kv. & Nair, Kc. Alginate impressions: A practical perspective. *J. Conserv. Dent.* **11**, 37 (2008). doi.10.4103/0972-0707.43416.

21. Huse, R. O., Quinten Ruhe, P., Wolke, J. G. C. & Jansen, J. A. The use of porous calcium phosphate scaffolds with transforming growth factor beta 1 as an onlay bone graft substitute. *Clin. Oral Implants Res.* **15**, 741–749 (2004). doi.10.1111/j.1600-0501.2004.01068.x.

22. Zhang, H.-X. *et al.* Biocompatibility and osteogenesis of calcium phosphate composite scaffolds containing simvastatin-loaded PLGA microspheres for bone tissue engineering. *J. Biomed. Mater. Res. A* **103**, 3250–3258 (2015). doi.10.1002/jbm.a.35463.

23. Lowe, B. *et al.* The regenerative applicability of bioactive glass and beta-tricalcium phosphate in bone tissue engineering: A transformation perspective. *J. Funct. Biomater.* **10**, 1–18 (2019). doi.10.3390/jfb10010016.

24. Farid, S. B. H. *Structure, microstructure, and properties of bioceramics*. *Bioceramics: For Materials Science and Engineering* (2019). doi:10.1016/b978-0-08-102233-7.00002-1. doi.10.1016/b978-0-08-102233-7.00002-1.

25. Koschwanez, H. E. & Reichert, W. M. *Textured and Porous Materials*. *Biomaterials Science: An Introduction to Materials: Third Edition* (Elsevier, 2013). doi:10.1016/B978-0-08-087780-8.00030-9. doi.10.1016/B978-0-08-087780-8.00030-9.

26. Combes, C. & Rey, C. Adsorption of proteins and calcium phosphate materials bioactivity. *Biomaterials* **23**, 2817–2823 (2002). doi.10.1016/S0142-9612(02)00073-X.

27. Sharpe, J. R., Sammons, R. L. & Marquis, P. M. Effect of pH on protein adsorption to hydroxyapatite and tricalcium phosphate ceramics. *Biomaterials* **18**, 471–476 (1997). doi.10.1016/S0142-9612(96)00157-3.

28. Rouahi, M., Champion, E., Gallet, O., Jada, A. & Anselme, K. Physico-chemical characteristics and protein adsorption potential of hydroxyapatite particles: Influence on in vitro biocompatibility of ceramics after sintering. *Colloids Surfaces B Biointerfaces* **47**, 10–19 (2006). doi.10.1016/j.colsurfb.2005.11.015.

29. Liu, H. S. *et al.* Hydroxyapatite synthesized by a simplified hydrothermal method. *Ceram. Int.* **23**, 19–25 (1997). doi.10.1016/0272-8842(95)00135-2.

30. Nandi, S. K. *et al.* Orthopaedic applications of bone graft & graft substitutes: a review. *Indian J. Med. Res.* **132**, 15–30 (2010).

31. Włodarski, K. H., Włodarski, P. K. & Galus, R. Bioactive composites for bone regeneration. Review. *Ortop. Traumatol. Rehabil.* **10**, 201–210 (2008).

32. Sadat-Shojai, M., Khorasani, M. T., Dinpanah-Khoshdargi, E. & Jamshidi, A. Synthesis methods for nanosized hydroxyapatite with diverse structures. *Acta Biomater.* **9**, 7591–7621 (2013). doi.10.1016/j.actbio.2013.04.012.

33. Goto, T. *et al.* Resorption of synthetic porous hydroxyapatite and replacement by newly formed bone. *J. Orthop. Sci.* **6**, 444–447 (2001). doi.https://doi.org/10.1007/s007760170013.

34. Ito, M., Hidaka, Y., Nakajima, M., Yagasaki, H. & Kafrawy, A. H. Effect of hydroxyapatite content on physical properties and connective tissue reactions to a chitosan-hydroxyapatite composite membrane. *J. Biomed. Mater. Res.* **45**, 204–208 (1999). doi.10.1002/(sici)1097-4636(19990605)45:3<204::aid-jbm7>3.0.co;2-4.

35. Bohner, M., Galea, L. & Doebelin, N. Calcium phosphate bone graft substitutes: Failures and hopes. *J. Eur. Ceram. Soc.* **32**, 2663–2671 (2012). doi.10.1016/j.jeurceramsoc.2012.02.028.

36. Yonehara, Y., Takato, T., Hikiji, H., Suzuki, A. & Nakatsuka, T. Investigation of the biocompatibility and osteoinductive ability of a high porosity hydroxyapatite and tricalciumphosphate composite. **43**, 981–987 (2000).

37. Nair, M. B., Varma, H. K. & John, A. Triphasic ceramic coated hydroxyapatite as a niche for goat stem cell-derived osteoblasts for bone regeneration and repair. *J. Mater. Sci. Mater. Med.* **20**, 809–812 (2009). doi.10.1007/s10856-008-3598-8.

38. With, G., Dijk, H. J. A., Hattu, N. & Prijs, K. Preparation, microstructure and mechanical properties of dense polycrystalline hydroxy apatite. *J. Mater. Sci.* **16**, 1592–1598 (1981). doi.10.1007/bf00553971.

39. Habraken, W., Habibovic, P., Epple, M. & Bohner, M. Calcium phosphates in biomedical applications: Materials for the future? *Mater. Today* **19**, 69–87 (2016). doi.10.1016/j.mattod.2015.10.008.

40. Rosen, H. M. The response of porous hydroxyapatite to contiguous tissue infection. *Plast. Reconstr. Surg.* **88**, 1076—1080 (1991). doi.10.1097/00006534-199112000-00020.

41. Chidyllo, S. A. & Marschall, M. A. POROUS HYDROXYAPATITE AND TISSUE INFECTION. *Plast. Reconstr. Surg.* **90**, (1992).

42. Yamada, M., Shiota, M., Yamashita, Y. & Kasugai, S. Histological and histomorphometrical comparative study of the degradation and osteoconductive characteristics of α- and β-tricalcium phosphate in block grafts. *J. Biomed. Mater. Res. Part B Appl. Biomater.* **82B**, 139–148 (2007). doi.10.1002/jbm.b.30715.

43. Carrodeguas, R. G. & De Aza, S. α-Tricalcium phosphate: Synthesis, properties and biomedical applications. *Acta Biomater.* **7**, 3536–3546 (2011). doi.10.1016/j.actbio.2011.06.019.

44. Legeros, R. Z., Lin, S., Rohanizadeh, R., Mijares, D. & Legeros, J. P. Biphasic calcium phosphate bioceramics: Preparation, properties and applications. *J. Mater. Sci. Mater. Med.* **14**, 201–209 (2003). doi.10.1023/A:1022872421333.

45. Marques, C. F. *et al.* Novel sintering-free scaffolds obtained by additive manufacturing for concurrent bone regeneration and drug delivery: Proof of concept. *Mater. Sci. Eng. C* **94**, 426–436 (2019). doi.https://doi.org/10.1016/j.msec.2018.09.050.

46. Budiraharjo, R., Neoh, K. G. & Kang, E. T. Hydroxyapatite-coated carboxymethyl chitosan scaffolds for promoting osteoblast and stem cell differentiation. *J. Colloid Interface Sci.* **366**, 224–232 (2012). doi.10.1016/j.jcis.2011.09.072.

47. Sowmya, S., Bumgardener, J. D., Chennazhi, K. P., Nair, S. V. & Jayakumar, R. Role of nanostructured biopolymers and bioceramics in enamel, dentin and periodontal tissue regeneration. *Prog. Polym. Sci.* **38**, 1748–1772 (2013). doi.10.1016/j.progpolymsci.2013.05.005.

48. Hu, Y. *et al.* Biomimetic mineralized hierarchical hybrid scaffolds based on in situ synthesis of nano-hydroxyapatite/chitosan/chondroitin sulfate/hyaluronic acid for bone tissue engineering. *Colloids Surfaces B Biointerfaces* **157**, 93–100 (2017). doi.https://doi.org/10.1016/j.colsurfb.2017.05.059.

49. Meng, J. *et al.* Super-paramagnetic responsive nanofibrous scaffolds under static magnetic field enhance osteogenesis for bone repair in vivo. *Sci. Rep.* **3**, 1–7 (2013). doi.10.1038/srep02655.

50. Shuai, C. *et al.* Magnetically actuated bone scaffold: Microstructure, cell response and osteogenesis. *Compos. Part B Eng.* **192**, 107986 (2020). doi.10.1016/j.compositesb.2020.107986.

51. Mushtaq, F. *et al.* Magnetoelectric 3D scaffolds for enhanced bone cell proliferation. *Appl. Mater. Today* **16**, 290–300 (2019). doi.10.1016/j.apmt.2019.06.004.

52. Singh, R. K. *et al.* Potential of magnetic nanofiber scaffolds with mechanical and biological properties applicable for bone regeneration. *PLoS One* **9**, (2014). doi.10.1371/journal.pone.0091584.

53. Kuttappan, S., Mathew, D. & Nair, M. B. Biomimetic composite scaffolds containing bioceramics and collagen/gelatin for bone tissue engineering - A mini review. *Int. J. Biol. Macromol.* **93**, 1390–1401 (2016). doi.10.1016/j.ijbiomac.2016.06.043.

54. Hamilton, P. T. *et al.* Improved Bone Morphogenetic Protein-2 Retention in an Injectable Collagen Matrix Using Bifunctional Peptides. *PLoS One* **8**, 1–10 (2013). doi.10.1371/journal.pone.0070715.

55. Tebyanian, H. *et al.* Effects of collagen/β-tricalcium phosphate bone graft to regenerate bone in critically sized rabbit calvarial defects. *J. Appl. Biomater. Funct. Mater.* **17**, (2019). doi.10.1177/2280800018820490.

56. Gloria, A. *et al.* Magnetic poly(1-caprolactone)/irondoped hydroxyapatite nanocomposite substrates for advanced bone tissue engineering. *J. R. Soc. Interface* **10**, (2013). doi.10.1098/rsif.2012.0833.

57. Perez, R. A. & Ginebra, M. P. Injectable collagen/α-tricalcium phosphate cement: Collagen-mineral phase interactions and cell response. *J. Mater. Sci. Mater. Med.* **24**, 381–393 (2013). doi.10.1007/s10856-012-4799-8.

58. Xia, Y. *et al.* Selective laser sintering fabrication of nano-hydroxyapatite/poly-ε-caprolactone scaffolds for bone tissue engineering applications. *Int. J. Nanomedicine* **8**, 4197–4213 (2013). doi.10.2147/IJN.S50685.

59. Milovac, D., Gallego Ferrer, G., Ivankovic, M. & Ivankovic, H. PCL-coated hydroxyapatite scaffold derived from cuttlefish bone: Morphology, mechanical properties and bioactivity. *Mater. Sci. Eng. C* **34**, 437–445 (2014). doi.10.1016/j.msec.2013.09.036.

60. der Vis, H. M., Aspenberg, P., Marti, R. K., Tigchelaar, W. & Van Noorden, C. J. Fluid pressure causes bone resorption in a rabbit model of prosthetic loosening. *Clin. Orthop. Relat. Res.* 201—208 (1998).

61. Mouzin, O., Sballe, K. & Bechtold, J. E. Loading improves anchorage of hydroxyapatite implants more than titanium implants. *J. Biomed. Mater. Res.* **58**, 61–68 (2001). doi.10.1002/1097-4636(2001)58:1<61::AID-JBM90>3.0.CO;2-S.

62. Leucht, P. *et al.* Effect of mechanical stimuli on skeletal regeneration around implants. *Bone* **40**, 919–930 (2007). doi.10.1016/j.bone.2006.10.027.

63. Chao, E. Y. S., Inoue, N., Ripamonti, U. & Fenwick, S. Biophysical stimulation of bone fracture repair, regeneration and remodelling. *Eur. Cells Mater.* **6**, 72–85 (2003). doi.10.22203/eCM.v006a07.

64. Fernandez de Grado, G. *et al.* Bone substitutes: a review of their characteristics, clinical use, and perspectives for large bone defects management. *J. Tissue Eng.* **9**, (2018). doi.10.1177/2041731418776819.

65. Yu, H. *et al.* Improved tissue-engineered bone regeneration by endothelial cell mediated vascularization. *Biomaterials* **30**, 508–517 (2009). doi.10.1016/j.biomaterials.2008.09.047.

66. Lee, K., Silva, E. A. & Mooney, D. J. Growth factor delivery-based tissue engineering: General approaches and a review of recent developments. *J. R. Soc. Interface* **8**, 153–170 (2011). doi.10.1098/rsif.2010.0223.

67. Fini, M., Giavaresi, G., Giardino, R., Cavani, F. & Cadossi, R. Histomorphometric and mechanical analysis of the hydroxyapatite-bone interface after electromagnetic stimulation. An experimental study in rabbits. *J. Bone Jt. Surg. - Ser. B* **88**, 123–128 (2006). doi.10.1302/0301-620X.88B1.16496.

68. Lind, M. Growth factor stimulation of bone healing. Effects on osteoblasts, osteomies, and implants fixation. *Acta Orthop. Scand. Suppl.* **69**, (1998). doi.10.1080/17453674.1998.11744808.

69. Yuan, Z. *et al.* Development of a 3D Collagen Model for the In Vitro Evaluation of Magnetic-assisted Osteogenesis. *Sci. Rep.* **8**, 1–11 (2018). doi.10.1038/s41598-018-33455-2.

70. Fini, M. *et al.* The effect of pulsed electromagnetic fields on the osteointegration of hydroxyapatite implants in cancellous bone: A morphologic and microstructural in vivo study. *J. Orthop. Res.* **20**, 756–763 (2002). doi.10.1016/S0736-0266(01)00158-9.

71. Robling, A. G., Burr, D. B. & Turner, C. H. Recovery periods restore mechanosensitivity to dynamically loaded bone. *J. Exp. Biol.* **204**, 3389–3399 (2001).

72. Dashnyam, K., Perez, R. A., Singh, R. K., Lee, E.-J. & Kim, H.-W. Hybrid magnetic scaffolds of gelatin–siloxane incorporated with magnetite nanoparticles effective for bone tissue engineering. *RSC Adv.* **4**, 40841–40851 (2014). doi.10.1039/C4RA06621A.

73. Inoue, N. *et al.* Effect of pulsed electromagnetic fields (PEMF) on late-phase osteotomy gap healing in a canine tibial model. *J. Orthop. Res.* **20**, 1106–1114 (2002). doi.10.1016/S0736-0266(02)00031-1.

74. Mammi, G. I., Rocchi, R., Cadossi, R., Massari, L. & Traina, G. C. The electrical stimulation of tibial osteotomies. Double-blind study. *Clin. Orthop. Relat. Res.* 246—253 (1993).

75. Yang, J., Zhang, J., Ding, C., Dong, D. & Shang, P. Regulation of Osteoblast Differentiation and Iron Content in MC3T3-E1 Cells by Static Magnetic Field with Different Intensities. *Biol. Trace Elem. Res.* **184**, 214–225 (2018). doi.10.1007/s12011-017-1161-5.

76. Sakurai, T., Terashima, S. & Miyakoshi, J. Enhanced secretion of prostaglandin E2 from osteoblasts by exposure to a strong static magnetic field. *Bioelectromagnetics* **29**, 277–283 (2008). doi.10.1002/bem.20392.

77. Protection, I. C. on N.-I. R. GUIDELINES ON LIMITS OF EXPOSURE TO STATIC MAGNETIC FIELDS.

Health Phys. **96**, (2009).

78. Yun, H. M. *et al.* Magnetic nanocomposite scaffolds combined with static magnetic field in the stimulation of osteoblastic differentiation and bone formation. *Biomaterials* **85**, 88–98 (2016). doi.10.1016/j.biomaterials.2016.01.035.

79. Panseri, S. *et al.* Magnetic Hydroxyapatite bone substitutes to enhance tissue regeneration: Evaluation in vitro using osteoblast-like cells and in vivo in a bone defect. *PLoS One* **7**, 4–11 (2012). doi.10.1371/journal.pone.0038710.

80. Xia, Y. *et al.* Novel magnetic calcium phosphate-stem cell construct with magnetic field enhances osteogenic differentiation and bone tissue engineering. *Mater. Sci. Eng. C* **98**, 30–41 (2019). doi.10.1016/j.msec.2018.12.120.

81. Meng, S., Rouabhia, M. & Zhang, Z. Electrical stimulation modulates osteoblast proliferation and bone protein production through heparin-bioactivated conductive scaffolds. *Bioelectromagnetics* **34**, 189–199 (2013). doi.10.1002/bem.21766.

82. He, J. *et al.* A magnetic hydroxyapatite composite scaffoldbased magnetic therapy for bone repair: An experimental study in canis lupus familiaris. *Regen. Biomater.* **4**, 97–103 (2017). doi.10.1093/rb/rbw039.

83. Puricelli, E., Ulbrich, L. M., Ponzoni, D. & Filho, J. J. da C. Histological analysis of the effects of a static magnetic field on bone healing process in rat femurs. *Head Face Med.* **2**, 43 (2006). doi.10.1186/1746-160x-2-43.

84. Neuberger, T., Schöpf, B., Hofmann, H., Hofmann, M. & Von Rechenberg, B. Superparamagnetic nanoparticles for biomedical applications: Possibilities and limitations of a new drug delivery system. *J. Magn. Magn. Mater.* **293**, 483–496 (2005). doi.10.1016/j.jmmm.2005.01.064.

85. Dulińska-Litewka, J. *et al.* Superparamagnetic iron oxide nanoparticles-current and prospective medical applications. *Materials (Basel).* **12**, (2019). doi.10.3390/ma12040617.

86. Tampieri, A. *et al.* Intrinsic magnetism and hyperthermia in bioactive Fe-doped hydroxyapatite. *Acta Biomater.* **8**, 843–851 (2012). doi.10.1016/j.actbio.2011.09.032.

87. Sun, C., Lee, J. S. H. & Zhang, M. Magnetic nanoparticles in MR imaging and drug delivery. *Adv. Drug Deliv. Rev.* **60**, 1252–1265 (2008). doi.10.1016/j.addr.2008.03.018.

88. Bretcanu, O., Verné, E., Cöisson, M., Tiberto, P. & Allia, P. Magnetic properties of the ferrimagnetic glass-ceramics for hyperthermia. *J. Magn. Magn. Mater.* **305**, 529–533 (2006). doi.10.1016/j.jmmm.2006.02.264.

89. Arruebo, M., Fernández-Pacheco, R., Ibarra, M. R. & Santamaría, J. Magnetic nanoparticles for drug delivery The potential of magnetic NPs stems from the intrinsic properties of their magnetic cores combined with their drug loading capability and the biochemical properties that can be bestowed on them by means of a suitab. **2**, 22–32 (2007).

90. Amirfazli, A. Magnetic nanoparticles hit the target. *Nat. Nanotechnol.* **2**, 467–468 (2007). doi.10.1038/nnano.2007.234.

91. Jiang, M. *et al.* Fe2+/Fe3+ substitution in hydroxyapatite: Theory and experiment. *Phys. Rev. B - Condens. Matter Mater. Phys.* **66**, 1–15 (2002). doi.10.1103/PhysRevB.66.224107.

92. Evis, Z. & Webster, T. J. Nanosize hydroxyapatite: Doping with various ions. *Adv. Appl. Ceram.* **110**, 311–320 (2011). doi.10.1179/1743676110Y.0000000005.

93. Sheikh, L. *et al.* Traversing the profile of biomimetically nanoengineered iron substituted hydroxyapatite: Synthesis, characterization, property evaluation, and drug release modeling. *RSC Adv.* **8**, 19389–19401 (2018). doi.10.1039/c8ra01539b.

94. Predoi, D. *et al.* Development of iron-doped hydroxyapatite coatings. *Coatings* **11**, 1–18 (2021). doi.10.3390/coatings11020186.

95. Lin, T. C., Lin, F. H. & Lin, J. C. In vitro feasibility study of the use of a magnetic electrospun chitosan nanofiber composite for hyperthermia treatment of tumor cells. *Acta Biomater.* **8**, 2704–2711 (2012). doi.10.1016/j.actbio.2012.03.045.

96. Cunha, C., Panseri, S., Marcacci, M. & Tampieri, A. Evaluation of the Effects of a Moderate Intensity Static Magnetic Field Application on Human Osteoblast-Like Cells. *Am. J. Biomed. Eng.* **2**, 263–268 (2013). doi.10.5923/j.ajbe.20120206.05.

97. Kim, E. C. *et al.* Effects of moderate intensity static magnetic fields on human bone marrow-derived mesenchymal stem cells. *Bioelectromagnetics* **36**, 267–276 (2015). doi.10.1002/bem.21903.

98. Harada, S. I. & Rodan, G. A. Control of osteoblast function and regulation of bone mass. *Nature* **423**, 349–355 (2003). doi.10.1038/nature01660.

99. Zhuang, J., Lin, S., Dong, L., Cheng, K. & Weng, W. Magnetically actuated mechanical stimuli on Fe 3 O 4 /mineralized collagen coatings to enhance osteogenic differentiation of the MC3T3-E1 cells. *Acta Biomater.* **71**, 49–60 (2018). doi.10.1016/j.actbio.2018.03.009.

100. Cezar, C. A. *et al.* Biphasic Ferrogels for Triggered Drug and Cell Delivery. *Adv. Healthc. Mater.* **3**, 1869–1876 (2014). doi.10.1002/adhm.201400095.

101. Ying Kei, C. L. *Iron-substituted hydroxyapatite*. *Handbook of Ionic Substituted Hydroxyapatites* (Elsevier Ltd, 2019). doi:10.1016/B978-0-08-102834-6.00011-2. doi.10.1016/B978-0-08-102834-6.00011-2.

102. Panseri, S. *et al.* Intrinsically superparamagnetic Fe-hydroxyapatite nanoparticles positively influence osteoblast-like cell behaviour. *J. Nanobiotechnology* **10**, 1–10 (2012). doi.10.1186/1477-3155-10-32.

103. Park, J. Y., Choi, E. S., Baek, M. J. & Lee, G. H. Colloidal stability of amino acid coated magnetite nanoparticles in physiological fluid. *Mater. Lett.* **63**, 379–381 (2009). doi.10.1016/j.matlet.2008.10.057.

104. Nayak, B. & Misra, P. K. Recognition of the surface characteristics and electrical properties of a nanocrystalline hydroxyapatite synthesized from Pila globosa shells for versatile applications. *Mater. Chem. Phys.* **230**, 187–196 (2019). doi.10.1016/j.matchemphys.2019.03.068.

105. Laranjeira, M. S. *et al.* Different hydroxyapatite magnetic nanoparticles for medical imaging: Its effects on hemostatic, hemolytic activity and cellular cytotoxicity. *Colloids Surfaces B Biointerfaces* **146**, 363–374 (2016). doi.10.1016/j.colsurfb.2016.06.042.

106. Stojanović, Z., Veselinović, L., Marković, S., Ignjatović, N. & Uskoković, D. Hydrothermal synthesis of nanosized pure and cobalt-exchanged hydroxyapatite. *Mater. Manuf. Process.* **24**, 1096–1103 (2009). doi.10.1080/10426910903032113.

107. Laranjeira, M. S., Fernandes, M. H. & Monteiro, F. J. Innovative macroporous granules of nanostructured-hydroxyapatite agglomerates: Bioactivity and osteoblast-like cell behaviour. *J. Biomed. Mater. Res. - Part A* **95**, 891–900 (2010). doi.10.1002/jbm.a.32916.

108. Coelho, C. C., Sousa, S. R. & Monteiro, F. J. Heparinized nanohydroxyapatite/collagen granules for controlled release of vancomycin. *J. Biomed. Mater. Res. - Part A* **103**, 3128–3138 (2015). doi.10.1002/jbm.a.35454.

109. Liu, Y. *et al.* Novel template-casting technique for fabricating β-tricalcium phosphate scaffolds with high interconnectivity and mechanical strength and in vitro cell responses. *J. Biomed. Mater. Res. - Part A* **92**, 997–1006 (2010). doi.10.1002/jbm.a.32443.

110. Shuai, C., Li, P., Liu, J. & Peng, S. Optimization of TCP/HAP ratio for better properties of calcium phosphate scaffold via selective laser sintering. *Mater. Charact.* **77**, 23–31 (2013). doi.10.1016/j.matchar.2012.12.009.

111. Sabree, I., Gough, J. E. & Derby, B. Mechanical properties of porous ceramic scaffolds: Influence of internal dimensions. *Ceram. Int.* **41**, 8425–8432 (2015). doi.10.1016/j.ceramint.2015.03.044.

112. Gheisari, H., Karamian, E. & Abdellahi, M. A novel hydroxyapatite -Hardystonite nanocomposite ceramic. *Ceram. Int.* **41**, 5967–5975 (2015). doi.10.1016/j.ceramint.2015.01.033.

113. Li, W. *et al.* Static magnetic fields accelerate osteogenesis by regulating FLRT/BMP pathway. *Biochem. Biophys. Res. Commun.* **527**, 83–89 (2020). doi.10.1016/j.bbrc.2020.04.090.

114. Wang, S. *et al.* Electrospun laponite-doped poly(lactic-co-glycolic acid) nanofibers for osteogenic differentiation of human mesenchymal stem cells. *J. Mater. Chem.* **22**, 23357–23367 (2012). doi.10.1039/C2JM34249A.

115. KAPLOW, L. S. A histochemical procedure for localizing and evaluating leukocyte alkaline phosphatase activity in smears of blood and marrow. *Blood* **10**, 1023–1029 (1955). doi.10.1182/blood.v10.10.1023.1023.

116. Tang, B. *et al.* Enhanced cellular osteogenic differentiation on CoFe2O4/P(VDF-TrFE) nanocomposite coatings under static magnetic field. *Colloids Surfaces B Biointerfaces* **198**, 111473 (2021). doi.10.1016/j.colsurfb.2020.111473.

6. Supplementary Material

1. Formulas Used for Stress and Strain Calculation

$$\sigma = \frac{F}{A}$$

σ is the stress (Pa)
F is the force (N)
A is the cross-sectional area (m2)

$$\varepsilon = \frac{\Delta L}{L_0}$$

ε is the strain (%)
L is the length (m)

2. Supporting table of the Resazurin Assay (Figure 18)

	Day 3	Day 7	Day 10
0MNP vs 0.5MNP	ns	ns	***
0MNP vs 1MNP	ns	*	**
0MNP vs 1.5 MNP	ns	***	****
0.5MNP vs 1MNP	ns	ns	ns
0.5MNP vs 1.5MNP	ns	ns	ns
1MNP vs 1.5MNP	ns	ns	ns
0MNP vs 0MNP+SMF	ns	ns	ns
0.5MNP vs 0.5MNP+SMF	***	ns	ns
1MNP vs 1MNP+SMF	***	ns	ns
1.5MNP vs 1.5MNP+SMF	**	**	ns
0.5MNP vs 0MNP+SMF	ns	ns	***
1MNP vs 0MNP+SMF	ns	*	**
1.5MNP vs 0MNP+SMF	ns	***	****

Table S1. Statistical analysis of the data of the Resazurin assay presented in Figure 18. The analysis was performed using one-way ANOVA, followed by the post hoc Tukey's test with significance level of $p < 0.05$. Statistically significant differences are marked with * ($p < 0.05$), ** ($p < 0.01$), *** ($p < 0.001$) or **** ($p < 0.0001$)